Loop Current attenuation after the Mid-Pleistocene Transition contributes to Northern hemisphere cooling

Christian Hübscher[a], Dirk Nürnberg[b]*

[a] Center for Earth System Research and Sustainability (CEN), Institute of Geophysics, University of Hamburg, Hamburg, Germany

[b] GEOMAR, Helmholtz Centre for Ocean Research Kiel, Kiel, Germany

* Corresponding author. Email: Christian.Huebscher@Uni-Hamburg.de

ORCID

C. Hübscher: 0000-0001-7380-2344

D. Nürnberg: 0000-0002-7136-1896

This is a Preprint which is currently under review at *Marine Geology (Elsevier)*. This is version 2 of this Preprint.

Highlights:

- First high-resolution seismic imagery from eastern Campeche Bank (Gulf of Mexico).
- The Chicxulub impact at K-Pg boundary caused mass failure of a length of ca. 150 km.
- Loop Current strength decreases since early MPT.
- Loop Current weakening contributed to northern hemisphere cooling.

Abstract

The beginning of the Mid-Pleistocene Transition (MPT) ~920 ka BP marked the expansion of northern hemisphere ice shields and caused a significant climate change in NW Europe. The MPT ended with the establishment of the 100 kyr ice age cyclicity at ~640 ka BP, due to orbital eccentricity changes. Previous studies explained the northern hemisphere cooling by cooling of sea-surface temperatures, increased sea-ice cover and/or changes in the Atlantic Meridional Overturning Circulation (AMOC) strength. We here discuss very-high resolution parametric echosounder (Parasound) imagery and sediment core analytics from a plastered drift at the eastern Campeche Bank (southern Gulf of Mexico), which was deposited under the influence of the Loop Current (LC). The LC transports warm tropical waters from the Caribbean into the Gulf via the Yucatan Channel. It is a key component of the Gulf Stream system, driving the ocean heat, salinity, and moisture transport towards the N Atlantic. The joint interpretation of reflection patterns, age constraints from color-scanning, foraminiferal stable oxygen isotopes, Sr isotope ratios ($^{87}Sr/^{86}Sr$) and core-seismic integration led to consistent conclusions about changes in LC strength across the MPT, thereby modulating the deep base level and the deposition of the plastered drift. The development of offlapping or onlapping plastered drifts, or the transition between the two termination patterns is best explained by changes in the depth of the relative deep base level and interpreted by changes in the flow regime.

Initially, the Middle Miocene to Pliocene closure of the Central American Seaway caused the onset and intensification of the LC and hence a deep base level fall. The sedimentary deposits from this phase have an offlapping prograding clinoform configuration, resembling a forced regression systems tract as is known from shelf areas. The deep base level fall caused sediment truncation above 500 m present day water depth. Below 500-550 m, the offlapping succession is overlain by sigmoidal and onlapping, transgressive systems tract like clinoforms. The transition from deep base level fall prior to the MPT to deep base level rise documents the weakening of the LC during the early MPT. After the MPT, the LC continued to weaken. The related reduction of heat transport from the Western Atlantic Warm Water Pool into the North Atlantic contributes to the further cooling of the northern hemisphere. Generally, the development of offlapping or onlapping plastered drifts or the transition between the two termination patterns can be explained by changes in the depth of the relative deep base level and interpreted by changes in the flow regime.

Keywords

Gulf of Mexico, paleoceanography, seismic, micropaleontology, plastered drift, Chicxulub impact

1. Introduction

The Atlantic meridional overturning circulation (AMOC) influences the North Atlantic hydrography, heat balance, and finally the climate in NW Europe (Schott et al., 1988; Molinari et al., 1990; Schmitz and Richardson, 1991; Nürnberg et al., 2008). The expansion of northern hemisphere ice shields at the beginning of the Mid-Pleistocene transition (MPT) ~920 ka BP (Mudelsee and Schulz, 1990) caused a significant climate change in NW Europe. The MPT ended with the establishment of the 100 kyr ice age cyclicity at ~640 ka BP, caused by orbital eccentricity changes (Pisias and Moore, 1981; Prell, 1982; Ruddiman et al., 1989) (Fig. 1). The reason for the 280 kyr delay of 100 kyr cyclicity remains enigmatic. The neglectable variability of orbital forcing cannot account alone for the dominance of 100 kyr-period oscillations in the climate system (Imbrie et al., 1993).

Several proxys indicate significant changes in the deep-water circulation in association with the MPT (for an overview see Tachikawa et al., 2020, and references therein). Schmieder et al. (2000), for example, concluded from a high-resolution Pleistocene magnetic susceptibility time series from the subtropical South Atlantic that dissolution driven variations in carbonate accumulation were controlled by deep water circulation changes. They assumed that the MPT was a discrete state of the Pleistocene deep-water circulation and climate system, terminated at ~540-530 ka. Nd isotope analysis by Pena and Goldstein (2014) pointed to a major disruption of the South Atlantic thermohaline circulation (THC) system during the MPT between Marine Isotope Stage (MIS) 25 and MIS 21 from ~950 to ~860 ka BP, with a significant weakening during MIS 23 (~900 ka BP). After the MPT, the glacial deep-water circulation continued to remain relatively weak during the glacials. Kim et al. (2021) also used Nd isotopes to confirm this interpretation for the North Atlantic, proving that this “MPT-AMOC crisis” occurred basin wide. Pena and Goldstein (2014) stated that the MPT ocean circulation crisis facilitated the coeval drawdown of atmospheric CO_2 (Hönisch et al., 2009) and subsequent high-latitude ice sheet buildup. Kaiser et al. (2019) concluded on enhanced northward advection of warm water during MIS 22 to 21 by interpreting the coiling direction of planktic foraminifer.

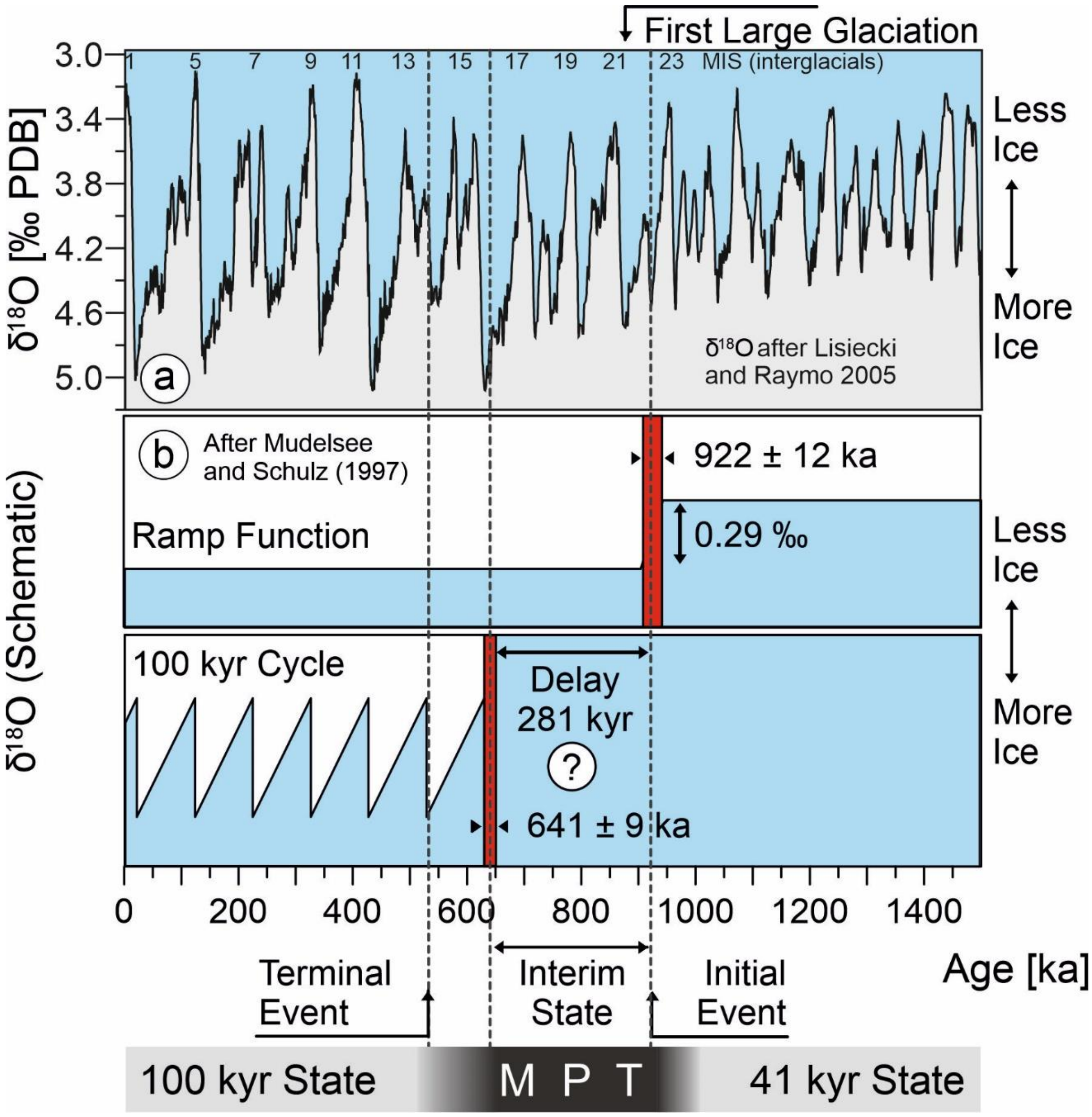

Fig. 1: Chronology of the Mid-Pleistocene climate transition (after Schmieder et al. 2000). Shift in mean and lagged onset of 100 kyr cyclicity of global ice volume (a) reflected in the stacked $\delta^{18}O$ global reference record (Lisiecki and Raymo, 2005) and (b) schematic view of the Mid-Pleistocene Climate Transition schematized after Mudelsee and Schulz (1997).

The Loop Current (LC), a prominent component of both the western boundary current system of the North Atlantic and the basin- to global-scale meridional overturning system dominates the surface and subsurface circulation in the Yucatan Strait and the Gulf of Mexico (Sturges and Evans, 1983; Zavala-Hidalgo et al., 2006) (Fig. 2a). The LC exits the Gulf of Mexico through the Florida Straits before entering the North Atlantic (Johns et al., 2002; Ezer et al., 2003; Oey et al., 2003; Oey 2004). As part of the Gulf Stream system, the LC represents a key element of the AMOC.

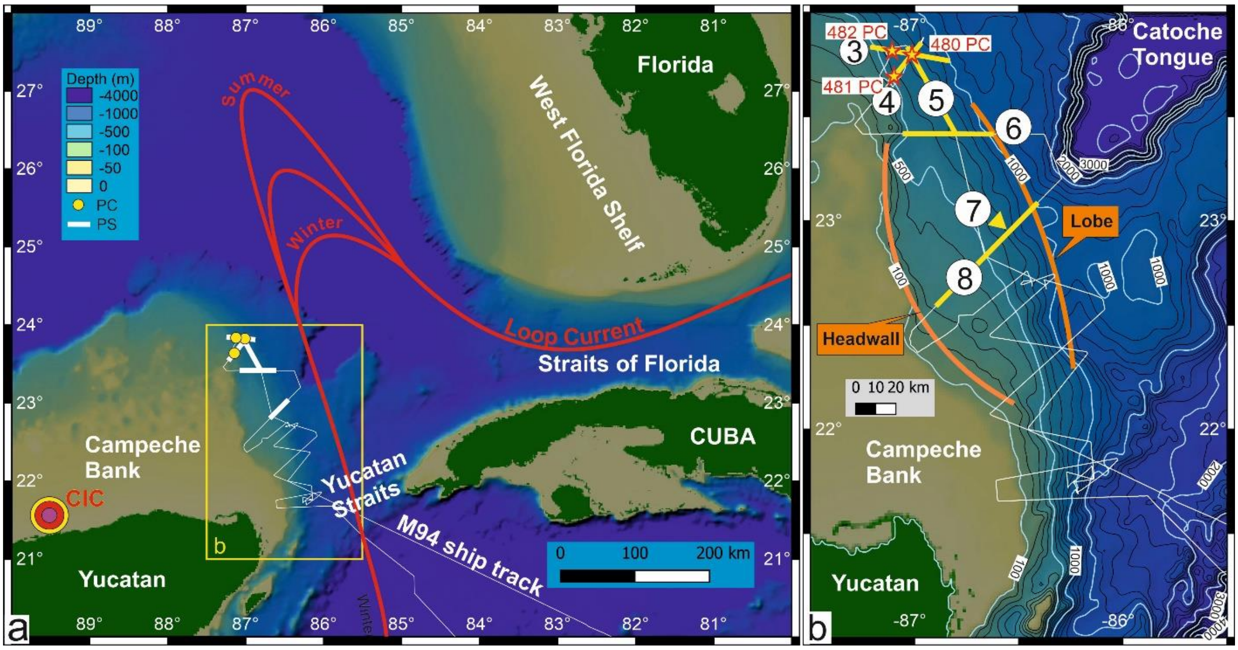

*Fig. 2: (a) Bathymetric map of southern Gulf of Mexico with adjacent Yucatan and Florida straits. The red lines indicate the simplified Loop Current during different seasons. Thin white line indicates M94 track (Hübscher et al., 2013). CIC = Chicxulub impact crater (*Paull et al., 2014). *(b) M94 cruise track (white lines), core sites (star symbols) and seismic profiles 3-8 (yellow lines), which correspond to the figures 3-8. Isobaths are plotted at 100 m intervals. PC = piston core; PS = Parasound. Bathymetric dataset: ETOPO1 (Amante et al., 2009).*

Hübscher et al. (2010) studied the impact of LC-related bottom currents on the upper slope sediments of the north-eastern Campeche Bank, Gulf of Mexico (Figs. 2a, 3). Sediment subbottom profiler data revealed a prominent unconformity (or disconformity) in water depth between 600 and ~680 m depth. They concluded that the transition from wavy reflection patterns in the lower succession to parallel planar reflections above, separated by a prominent unconformity, was caused by a change in LC strength at intermediate water depths. At that time, the lack of chronological constraints did not allow to unequivocally link LC variability to climate change.

This study is motivated by the validation of the working hypothesis that the inferred LC variability is related to the MPT and that a close relationship exists between changes in

THC strength (Fig. 1) and LC vigor (i.e. Hübscher et al., 2010). The data and samples were collected during RV METEOR expedition M94 in 2013 (Hübscher et al., 2014). Parametric sediment sub-bottom profiler transects and piston cores collected along the Campeche Bank (Fig. 2b) allow a detailed view on the temporal and spatial development of the unconformity initially described by Hübscher et al., (2010) and hence, the evolution of the Yucatan Strait throughflow since the MPT.

2. Regional Setting

The Gulf of Mexico is a semi-enclosed basin, which is framed by wide and shallow intertidal shelf areas (<20 m water depth; Fig. 2a). The study area is the north-eastern and eastern Campeche Bank. This massive and broad carbonate bank located north of the Yucatan Peninsula evolved until the mid-Cretaceous (Ordonez, 1936), and appears geologically similar to the southern Florida platform (e.g., Antoine and Ewing, 1963; Uchupi and Emery, 1968). Paull et al. (2014) related a steep cliff at the lower escarpment of the northern Campeche Bank to the Chicxulub impact close to the Cretaceous–Paleogene (K-Pg) transition. The joint interpretation of bathymetric maps and seismic data provided a clear line of evidence that the impact caused catastrophic mass wasting at the continental shelf adjacent to the escarpment due to the ground shaking.

Some general conclusions about sedimentation pattern on the eastern Campeche Bank since the K-Pg boundary can be derived from the western Florida shelf. Building on Mullins et al. (1987; 1988), Gardulski et al. (1991) explain the depositional patterns there by the amplification of the LC since the middle to late Miocene by the closure of the Panama Isthmus. For a detailed discussion of different time constrains for the closure see O´Dea et al. (2016) and references therein.

Near-surface sediments at the north-eastern Campeche Bank and the western Florida Slope consist mainly of calcareous ooze with >75 % of carbonate (Balsam and Beeson 2003; Hübscher et al., 2014), being shaped by the different currents in the Yucatan Channel between Yucatan and Cuba. Regarding the northbound flow, Sheinbaum et al. (2002) distinguished between the northward flowing northerly surface Yucatan Current and its southerly under-current off Mexico, and the southerly surface Cuban Counter-current near Cuba. Within the Gulf of Mexico, the ocean current system is termed LC. Paleoceanographic proxy records from the area reveal a close relationship between the LC dynamics, marine productivity, sea-surface temperature and salinity, and Mississippi discharge on centennial to orbital timescales (Emiliani, 1975; Gardulski et al., 1990; Nürnberg et al., 2008, 2015; Ziegler et al., 2008; Kujau et al., 2010).

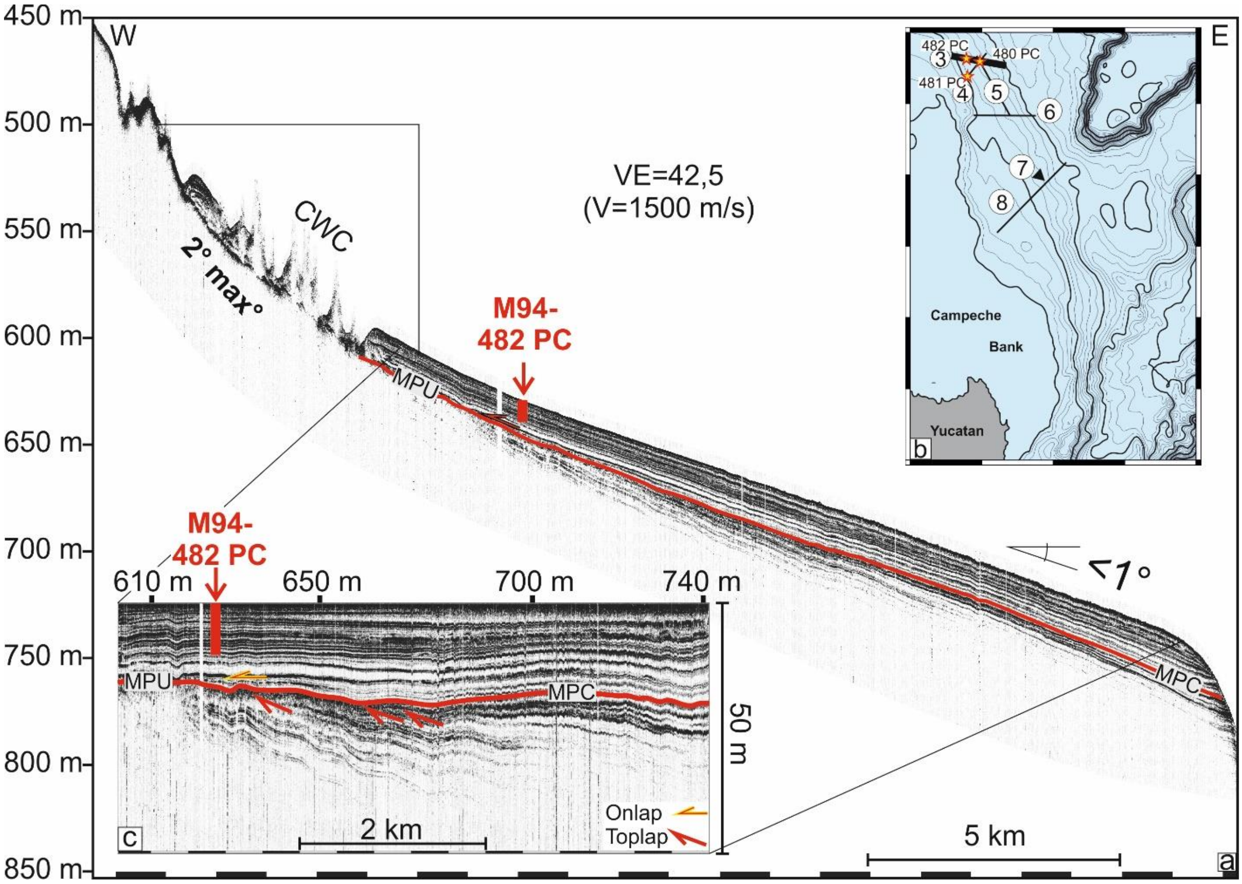

Fig. 3: (a) Parasound profile 3 collected during RV Meteor expedition M78/1 (Hübscher and Pulm, 2009) from eastern Campeche Bank (Hübscher et al., 2010) with location of piston core M94-482 PC. Core length has been calculated with a sound velocity of 1.5 m/ms, which might be too low (see chapter 5 for discussion). (b) Bathymetric map of study area (see also Fig. 2b) (c) Flattened profile of lower eastern Campeche Bank slope (for explanation see Chapter 3). CWC = Cold-water coral; MPU = Mid-Pleistocene Unconformity; MPC = Mid-Pleistocene Correlated Conformity (MPC); VE = vertical exaggeration.

Based on studies by Merino (1997), Rivas et al. (2005) and Hebbeln et al. (2014), Matos et al. (2017) characterized the local oceanography by five water masses. The Caribbean Surface Water (CSW) is transported northward at depths shallower than ~80 m. Below, a salinity maximum at ~100–160 m water depth characterizes the core of the Subtropical Intermediate Water. The Tropical Atlantic Central Water (TACW) exhibits an oxygen minimum at ~500 m water depth. The salinity minimum identifies the upper boundary of the Antarctic Intermediate Water (AAIW) at ~540 m water depth. The North Atlantic Deep Water (NADW) is present at water depths deeper than 1000 m.

Hübscher et al. (2010) discovered a Cold Water Coral (CWC) province along the north-eastern Campeche Bank (Fig. 3), mainly composed of *Enallopsammia profunda*–*Lophelia pertusa*, which was subsequently mapped in detail between 23°47'N and 23°54'N (Hebbeln et al., 2014; Matos et al., 2017). The Campeche CWC province is affected by the SE-NW directed LC (Fig. 1), which is strongest at surface (< 130 m water depth; 74–83 cm/s), while its eddies reach much deeper water (Hebbeln et al., 2014). At water depths of ~500-600 m, the prominent Campeche CWC mounds occur, enduring bottom velocities of ~30 cm/s (Hebbeln et al., 2014). A strong density gradient described at ~520–540 m is attributed to the boundary (pycnocline) between TACW and AAIW (Matos et al., 2017). Based on observed undulating isotherms, Hebbeln et al. (2014) hypothesized the presence of internal waves in that water depth. According to Matos et al. (2017), the pycnocline was absent during the glacial time periods of substantially lowered sea level.

The Gulf of Mexico as the northern part of the western Atlantic warm water pool is an important oceanic heat source, providing ocean heat towards the North Atlantic via the Gulf Stream System, thus acting as a key area in the global climate system. The LC as part of the Gulf Stream system dominates the surface and subsurface flow in the Gulf of Mexico (Sturges and Evans, 1983; Zavala-Hidalgo et al., 2006) (Fig. 2a). It comprises warm tropical waters that flow from the Caribbean into the Gulf through the Yucatan Channel and some distance towards the north, before shedding anticyclonic eddies (e.g., Oey, 2008, and references therein). The northward flow is compensated by a deep southbound counter flow into the Caribbean on both western and eastern lower slopes of the Yucatan Strait (Sheinbaum et al., 2002).

Two endmember modes characterize the northward extension of the LC. During summer, when the warm surface-water flow through the Yucatan Channel is enhanced, the LC may even reach the Mississippi river delta (Wiseman and Dinnel, 1988; Sheinbaum et al., 2002), thereby warming up the western and northern Gulf areas (Brunner et al., 1984). During winter, the LC flows almost directly from the Yucatan Channel to Florida Strait. During this phase, the northern Gulf remains rather unaffected by warm tropical surface water from the Caribbean. According to Ezer et al. (2003), the through-flow fluctuations in the Yucatan Channel largely correlate with the northward spreading of the LC.

3. Material and Methods

3.1 Bathymetry

Bathymetric measurements were carried out mainly with the hull mounted SIMRAD EM122 multi-beam system (Hübscher et al., 2014). This system emits periodically a swath of 256 preformed beams with signal frequencies of 12 kHz. The usable footprint of a single emitted swath perpendicular to the ship's heading has a width of larger than three times of the water depth. Due to the shallow water depth and the large distances between the profiles, the ETOPO1 data set (Amante et al., 2009) was used for the overview maps in Fig. 2 as well as for the insert maps of the seismic imagery.

3.2 Seismic imagery

The parametric sediment sub-bottom profiler (Parasound) system (PS) can be considered as a very high-resolution single channel seismic system. The Parasound emits two frequencies of 18 and 22 kHz (see Hübscher et al., 2010, and references there in). The parametric effect creates a narrow beam 4 kHz and 40 kHz signal within an opening angle of 4.5°. The sampling frequency of the raw data is 96 kHz. In opposite to, e.g., airgun seismics, the wavelet is released as "pulse trains". This means that follow-up wavelets are emitted before a sea floor reflection has returned to the transducer. Therefore, sea floor multiples do not necessarily correspond to twice the two-way travel time (TWT) of the sea floor reflection, as known from conventional seismic. The 4 kHz signal reveals a wave length of ~0.4 m. Depending on the acoustic impedance of the sediments near the sea floor, the Parasound signal penetrates several tens of meters into the sea floor and allows the resolution of layers with a thickness of very few tens of centimeters. Further details on the method can be found in the Supplementary Material. All Parasound profile are labeled with a water depth calculated with a rounded velocity of an acoustic wave in water (1500 m/s), so the water depth is reasonably correct. It seems likely, that the velocity increases slightly with depth due to compaction, so the thickness of sedimentary layers is presumably underestimated and the deviation increases with burial depth and compaction. The depth to reflections below sea floor are calculated with a velocity of 1500 m/s to sea floor and 1500-1800 m/s below sea floor. Those depth values are named "total depth", are rounded to full 5 m and the uncertainty is estimated to be ± 5m, which is good enough for the discussion in this study. Stratigraphic correlation between individual profiles was done with KINGDOM software by IHS Markit.

Fig. 2b shows the M94 cruise track with the accomplished Parasound profiles, as well as the core sites. The profiles stretch for ~150 km across the northern Campeche Bank. Due to the lack in signal penetration, the profiles further south do not contribute to this study.

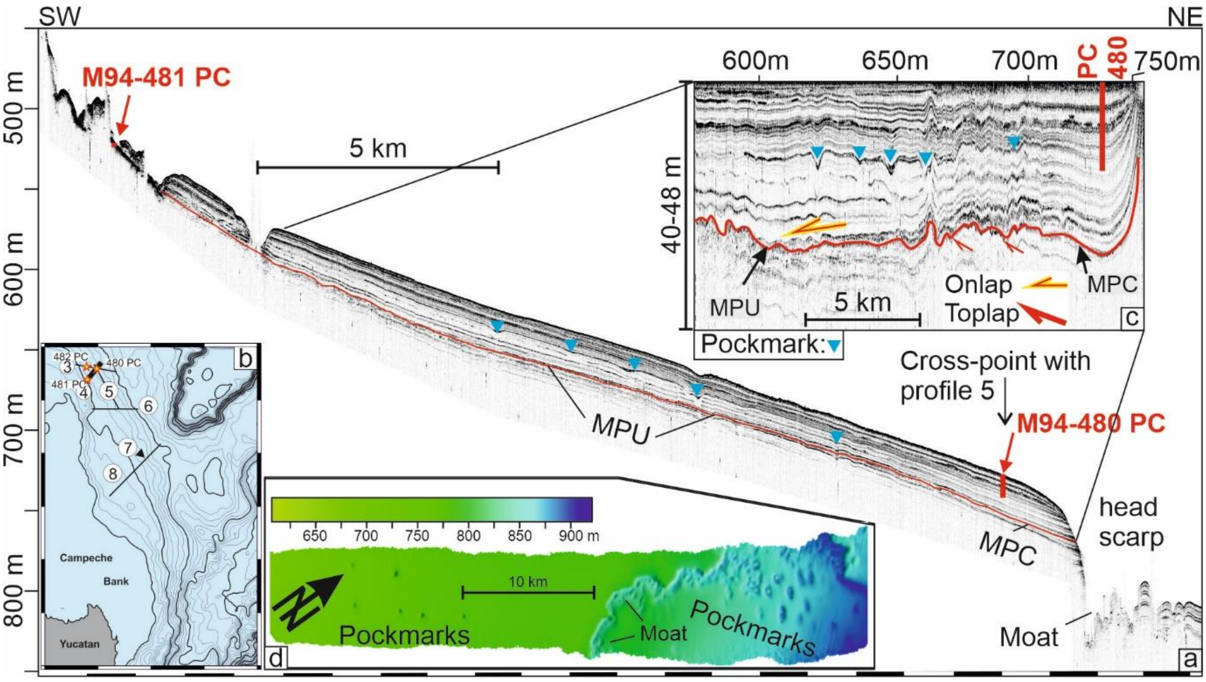

Fig. 4: (a) Parasound profile 4 (thick black line in b) with red line marking the Mid-Pleistocene Unconformity (MPU), which transforms into the correlated conformity (MPC). Piston core locations M94-480 PC and -481 PC and penetration depth are indicated. A black arrow marks the cross-point with profile 5 at site M94-480 PC. Core length calculated with 1.8 m/ms (see chapter 5 for discussion). For location see (b). (c) Flattened Parasound profile in detail. Blue arrows mark pockmarks. Note that the up-warping of the reflections at the north-eastern end of the flattened profile results from the truncation at the head scarp only. (d) Multi-beam (SIMRAD EM122) data showing pockmarks and moat along the head scarp. VE = vertical exaggeration.

3.3 Core sites

During research cruise M94, piston corers (PC) with core barrel lengths between 10 and 20 m were run. Although sea floor sediments were extremely hard to penetrate, and ship maneuvering was difficult due to up to 4 kn current speed, three deployments along the profile in Fig. 2 were successful.

Cores M94-480 PC and M94-481 PC were taken along the SW-NE striking profile 5, which well reflects the sedimentary features known from the M78/1 campaign (Hübscher et al., 2010; Fig. 3). Piston core M94-480 PC (23°48.141N 87°0.868W) was recovered from intermediate depths (~730 m) from the northeastern Campeche Bank penetrating the layered sequence of coarse to middle foraminiferal oozes, which become finer at greater depth (Fig. 4). Core recovery was ~12.2 m revealing undisturbed sediments of excellent quality (Appendix 2). Core M94-480 PC ended up in a horizon that reveals pockmarks (Fig. 4c).

The second 2.5 m long piston corer M94-481 PC (23°39.997N 87°7.284W) from the northern Campeche Bank transect is from ~521 m water depth, located in the mounded Campeche CWC complex (Fig. 4a). Core M94-481 PC mainly consists of an intercalated sequence of light foraminiferal ooze and sand, and darker foraminifera-rich shale/mudstone, reflecting glacial/interglacial-related sedimentological changes. Below this sequence at ~2.3 m core depth, the lithology changes into a very coarse-grained, diagenetically concreted sediment with sand-sized grains cemented into even larger particles ranging from a few millimeters to several centimeter. Large brachiopods up to 2-3 cm in length are abundant. The contact to the upper sediment is sharp.

The third piston core M94-482 PC (23°49.155N 87°7.752 W; ~7.8 m core recovery) was retrieved from ~630 m water depth, on the profile accomplished during M78 by Hübscher et al. (2010) (Fig. 3). Core M94-482 PC reveals the same sedimentary sequences as core M94-480 PC (Appendix 2), with a better preservation of the uppermost sediments.

3.4 Shipboard Core Logging: MINOLTA Color-Scanning

The MINOLTA CM-600d hand-held spectrophotometer was used onboard for color scanning of the freshly recovered sediment cores. The measurement of the light reflectance was done on the sediment surfaces of opened core sections. Routinely, the reflection data and standard color measurements were taken at 1 cm steps and were automatically recorded and processed by the software MINOLTA SpectraMagic v.2.3. The data are displayed in the L*, a* and b* CIELAB color coordinates. The L*-value represents brightness on a non-linear scale and can be directly correlated to grey value measurements. The a*-values indicate the relationship between green and magenta and the b*-value reflects blue/yellow colors. Further details on the method can be found in the Supplementary Material.

3.5 Foraminiferal Stable Oxygen and Carbon Isotopes

Stable oxygen ($\delta^{18}O$) isotope analyses were performed on a ThermoScientific MAT 253 mass spectrometer with an automated Kiel IV Carbonate Preparation Device at GEOMAR. The isotope values are calibrated versus the NBS19 (National Bureau of standards) carbonate standard and an in-house standard ("Standard Bremen"). Isotope values presented in the delta-notation are reported in permil (‰) relative to the VPDB (Vienna Peedee Belemnite) scale. The analytic precision is 0.06‰ for $\delta^{18}O$ and <0.03‰ for $\delta^{13}C$.

$\delta^{18}O$ measurements were made at 5 cm sample spacing for cores M84-480 and 482, and 2-3 cm sample spacing for core M84-481. $\delta^{18}O$ measurements were made on 2–3 specimens of the endobenthic foraminiferal species *Uvigerina* spp. from the 250–500 µm size fraction. The size fraction was chosen to eliminate redeposited tests of smaller specimens that may cause a bias of the benthic isotope signal (Lutze et al., 1979). According to Shackleton and Hall (1984), *Uvigerina* $\delta^{18}O$ values appear to be in equilibrium with seawater $\delta^{18}O$.

Additionally, $\delta^{18}O$ measurements were made on ~6 specimens of the planktonic foraminiferal species *Globigerinoides ruber* (white). The specimens are taken from the narrow-spaced size 355-400 µm size fraction in order to prevent bias due to ontogenetic variations (Lin et al., 1997). Due to its nearly uniform annual occurrence (Tedesco and Thunell, 2003), *G. ruber* shells are a standard tool for reconstructing past oceanic surface hydrography conditions, especially for glacial/interglacial changes in low-latitudes (Flower et al., 2004; Reissig et al., 2019; Nürnberg et al., 2021).

3.6 $^{87}Sr/^{86}Sr$ Method

Sr isotope ratios ($^{87}Sr/^{86}Sr$) of a brachiopod shell remain and enclosed residual sediment were determined by thermal ionization mass spectrometry (TIMS, TRITON, ThermoFisher Scientific) at GEOMAR. Additionally, on mm scale two distinct spots of the consolidated, underlying and shell-attached residual sediment were sub-sampled directly as powder with a diamond dental driller. All three samples dissolved completely in 2.25 N HNO_3 without siliciclastic remains. Further details on sample preparation can be found in the Supplementary Material.

Under clean lab conditions they were dried down and the actual SrSpec resin (Eichrom Technologies) based extraction, purification and measurement routines described in Schmidt et al. (2019) were applied. The measured isotope ratios were session specific normalized to the NIST SRM 987 value of 0.710248 according to Howarth and McArthur (2004) at a repeatability of ± 0.000006 (2SD, n=2). Potential influences of ^{87}Rb interferences on $^{87}Sr/^{86}Sr$ isotope ratios were eliminated by combining the highly selective Sr-Spec resin and Rb/Sr-discriminating TIMS preheating procedures with the static mode measurement of ^{85}Rb simultaneously with the Sr masses 84, 86, 87, and 88 for optional Rb/Sr corrections. As performance monitor an aliquot of the IAPSO seawater standard accompanied the whole procedure and resulted in 0.709173 ± 0.000008 (2 SEM) and acceptable accordance to a reference value of 0.709175 for modern seawater (Howarth and McArthur, 2004).

4. Results

4.1 Bathymetry

The Campeche Bank plateau reveals water depths of less than 100 m and a dip angle of <0.2° (Fig. 2). The 100 m and 200 m depth contours along the eastern bank form a nearly 200 km long arcuate terrain step with slope values up to 3°. As indicated by the increasing distance between the isobaths (Fig. 2b), the slope is flattened in water depth between 300 m and 600 m. In contrast to the 100 m and 200 m isobaths, the 600 m to 1000 m isobaths are convex-shaped downslope.

4.2 Seismic imagery

The Parasound profile 3 (Fig. 3) is a re-processed version of the data that were shown and described by Hübscher et al. (2010; their Fig. 9). In water depth above 520 m, the strong sea floor reflection allows no signal penetration. Further downslope, the pronounced seafloor mounds (~520-600 m water depth) are attributed to the CWC (*Lophelia*). As already mentioned by Hübscher et al. (2010), an unconformity and correlated conformity separates wavy reflections beneath from sub-parallel strata above. According to the hypothesis to be tested, the unconformity developed in the middle Pleistocene we adopt the following terminology (Fig. 3): (Fig. 3): MPU = Mid Pleistocene Unconformity; MPC = Mid Pleistocene Correlated Conformity, and MPU/C = the combined seismic interface.

The most basin-ward toplap beneath the MPU/C in a present-day water depth of ~660 m and 680±5 m total depth marks the lateral transition from MPU to MPC. In a total depth of ~655 m, the lowermost reflection above the MPU onlaps against it. In the flattened profile (Fig. 3c), the onlap appears as a downlap.

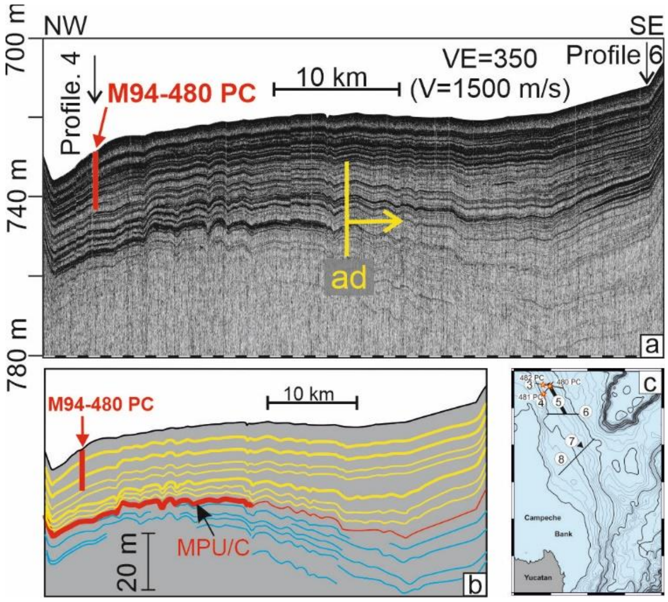

Fig. 5: (a) Parasound profile 5 and (b) according line drawing. Red line in (b) marks Mid-Pleistocene Unconformity and correlated conformity (MPU/C). PC480 labels piston core M94-480 PC, which is also the cross-point (black arrow) with the Parasound profile 4. Core length calculated with 1.8 m/ms (see chapter 5 for discussion). The cross-point with the Parasound profile 6 (black arrow to the right) is at the southeastern end of the profile. Note the southeastward amplitude decrease (ad) of reflections beneath ~12 m in the middle of the profile. VE = vertical exaggeration.

In order to link the new data from the M94 campaign to observations made by Hübscher et al. (2010) during the M78 expedition, the northernmost M94-profile 4 (Fig. 4) crosses the M78-profile 3, striking SW-NE and perpendicular to the continental slope. Stratified sediment sequences are evident below a water depth of ~520 m. Laterally traceable sediments are present only below ~570 m water depth. A head scarp at ~750 m water depth limits the occurrence of these deposits further downslope. As in profile 3, the MPU changes to the MPC at ~660 m water depth and 685±5 m total depth. The layers below the MPU/C and approximately the lower half of the sedimentary sequence above reflect rather diffusely. In contrast, the reflection horizons in the upper half are sharp and continuous. Also similar to profile 3, the lowermost reflection horizon above the MTU onlaps the unconformity. Lateral thickness variations become less moving upslope. Circular fluid escape structures (pockmarks) are present on the sea floor and on buried strata (Figs. 4c, d). Above the scarp, pockmarks at the seafloor reveal depths of up to ~40 m and diameters of ~200–260 m. Below the scarp, the pockmarks are elongated (Fig. 4d). Cross-sections of the buried pockmarks can be seen best in the flattened profile (Fig. 4c) and along a reflection horizon with an enhanced reflection amplitude. A moat channel runs in front of the scarp.

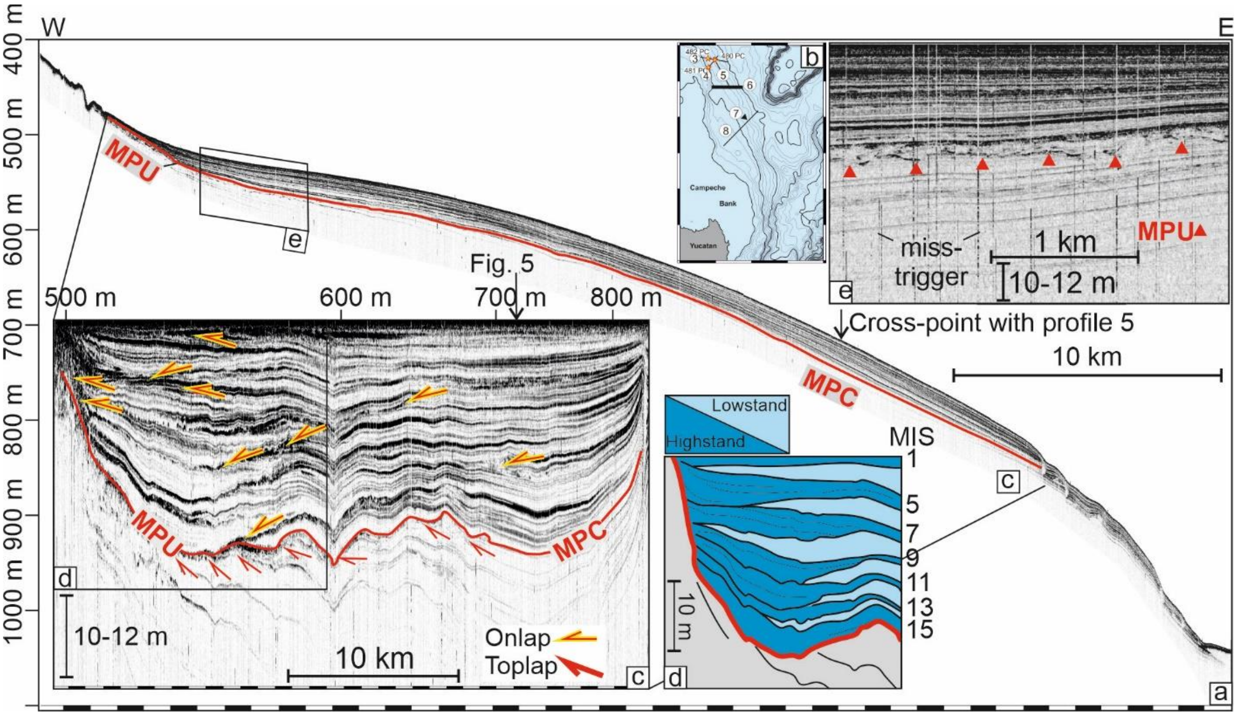

Fig. 6: (a) Parasound profile 6 running perpendicular to the continental slope. For location see insert map (b). Red line = Mid-Pleistocene Unconformity (MPU) and Correlated Conformity (MPC). Black arrow = cross-point with profile 5. (c) Flattened profile. Red arrows = onlaps and downlaps. (d) Line drawing with interpreted sea level highstand (dark blue), lowstand deposits (light blue) and suggested correlation with MIS. (e) Enlargement from upper slope. VE = vertical exaggeration.

The almost 50 km long Parasound profile 5 runs in water depths of ~705-740 m almost parallel to the bathymetric contour and rather perpendicular to Parasound profiles 3 and 4. The reflections are divergent to the southeast. Reflection terminations against MPU/C are not visible. The reflection amplitudes of the MPU/C abruptly decrease towards the SE, which occurs approximately, where the slope gradient flattens between 100 and 500

m water depth (Fig. 2b). The same applies to reflections in the lower half of the overlying layers. Reflections beneath the MPU/C are wavy and diverge southwards. Reflections directly above the MPU/C are also wavy. In a depth of ca. 12 m beneath the sea floor, reflection coefficients and thickness undulations generally decrease towards the SE.
The dip profile 6 is 45 km long and reveals a reflection pattern similar to profiles 3 and 4, which are30-40 km further north. Resolvable strata start to occur below 500 m water depth. The MPC could be stratigraphically linked to profile 3 and 4 by strike profile 5. In addition, the lowermost or most basin ward toplap marks the transition from the MPU to the MPC at ~680 m water depth and 710±5 m total depth. As seen best in the flattened profile (Fig. 6c), several onlap and downlap terminations are present above the MPU. The identification of reflection terminations allows recognizing 13 individual depositional units above the MPU, all marked in blue. Seven units onlap the MPU (dark blue), the other six are intercalated (light blue). In the shallower part (510-520 m water depth), the MPU separates reflections of low amplitude (below) from those with higher amplitudes. The blow-up in Fig. 6e elucidates the wavy truncation along the MPU.

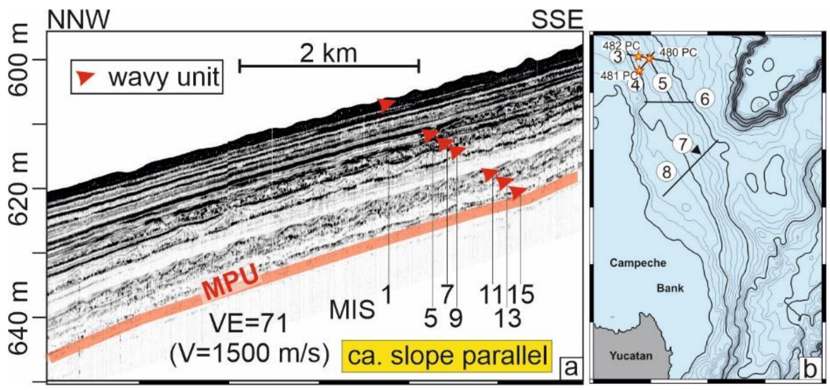

Fig. 7: (a) Parasound profile 7 almost parallel to the contour. (b) The profile 7 is too short to be resolved in the insert map. It runs almost parallel to the slope. The black triangle marks, where the profile stops at profile 8. Red line = Mid-Pleistocene Unconformity (MPU). Red arrows = wavy horizons and suggested correlation with MIS. VE = vertical exaggeration.

The overburden of the MPU condenses seventy kilometers further to the south, as shown in the blow-up of the NNW-SSE-striking profile 7. The sea floor and the uppermost less than a meter-thick unit is wavy, and so are six further units above the MPU. Between the uppermost and the 2nd wavy unit an approximately 8 m thick unit with parallel and continuous reflections is present.

The southernmost dip profile 8 elucidates the slope deposits where the dip angle of the upper slope is minimal (~0.5°) (Fig. 8a, b). The transition from MTC to MTU occurs ca. at 630 m water depth and 660±5 m total depth. The imaged strata below form oblique clinoforms, which are thickest at ~750 m water depth. The resolved strata toplap against the MPU upslope and converged further downslope. A diffusely reflecting layer a few meters thick, whose internal structure cannot be resolved, overlies the MPU upslope from about 600 m water depth. Younger units onlap against this diffusely reflecting layer but terminate upslope at ca. 520 m. Generally and along the entire profile, the strata overlying the MPU/C represent sigmoidal clinoforms. The lowermost clinoform onlaps the MPU at 600 m water depth and ca. 20 m beneath sea floor. At the upper slope, prograding sigmoidal clinoforms truncated in water depths shallower than 400 m (Fig. 8d).

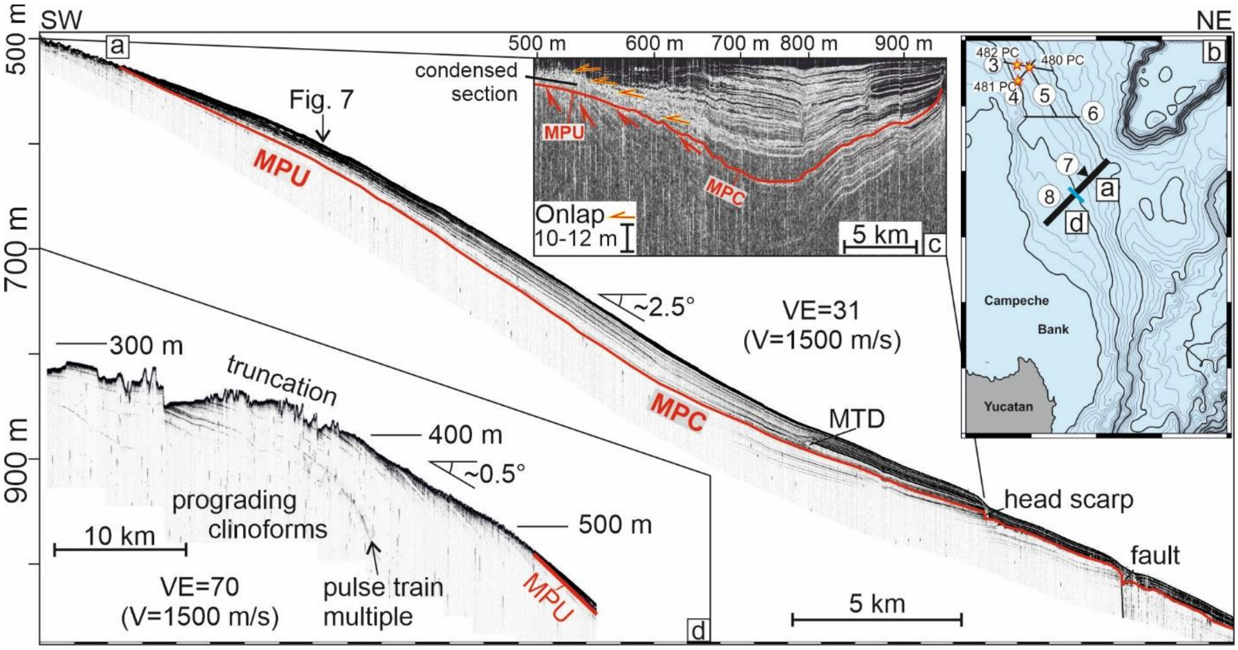

Fig. 8: (a) Parasound profile 8. Red line = Mid-Pleistocene Unconformity (MPU) and Correlated Conformity (MPC). Black arrow = cross-point with profile 7. For location see insert map (b). (c) Flattened profile with red arrows marking toplap terminations. The signal to noise ratio of internal reflection amplitudes is rather small. In order to identify reflection terminations and to distinguish between the MPU and the MPC, the grey scale colors are inverted. (d) Upslope prolongation of (a). Note the sea floor "pulse-train" multiple (see chapter 3.2 for explanation) and the different vertical exaggeration (VE) compared to (a).

4.3 Chronostratigraphy of sediment cores

The stratigraphic framework of cores M94-480 PC, -481 PC and -482 PC is based on a combination of stable oxygen isotope stratigraphy, orbital tuning, core correlation of sediment color data, and $^{87}Sr/^{86}Sr$ radiometric dating.

4.3.1 Strontium isotopes

The determined $^{87}Sr/^{86}Sr$ ratios of 0.709168 (± 0.000008) for the brachiopod shell fragment and the nearly identical values of 0.709157 (± 0.000009) and 0.709159 (± 0.000009) for the underlying residual sediment overlap within uncertainty. Especially taking into account the extreme similarity of the two latter implies a systematic difference to the shell fragment. Note, the given uncertainties include the propagation of the normalization repeatability (2SD level) on the 2 SEM uncertainty of the single sample measurements.

Table 1: Transfer of $^{87}Sr/^{86}Sr$ ratios into mean SIS ages and uncertainties. Numbers in brackets refer to the following remarks: (1) Brachiopd samples all from M94-481-PC. (2) $^{87}Sr/^{86}Sr$ normalized on NIST-SRM-987 ratio of 0.710248 according to Howarth and McArthur (2004). (3) Uncertainty applied for SIS age range determination based on propagation of normalization 2 SD on measurement 2 SEM. (3) 0.709175 reference values for modern seawater according Howarth and McArthur (2004).

Sample ident (1)	lab code	$^{87}Sr/^{86}Sr$ (2)	± (3) x 10^{-5}	SIS-Look-up 2004 mean age (Ma)	min age (Ma)	max age (Ma)
Brachiopod-enclosed matrix 1	207-13	0.709157	0.9	0.59	0.28	0.83
Brachiopod-enclosed matrix 2	208-13	0.709159	0.9	0.55	0.23	0.78
Brachiopod-shell2	209-13	0.709168	0.8	0.26	recent	0.57
(3) IAPSO-modern seawater std.	session-rel.	0.709173	0.8			
NIST SRM-987: of session / n=2 / 2 SD	session-rel.	0.710248	0.6			

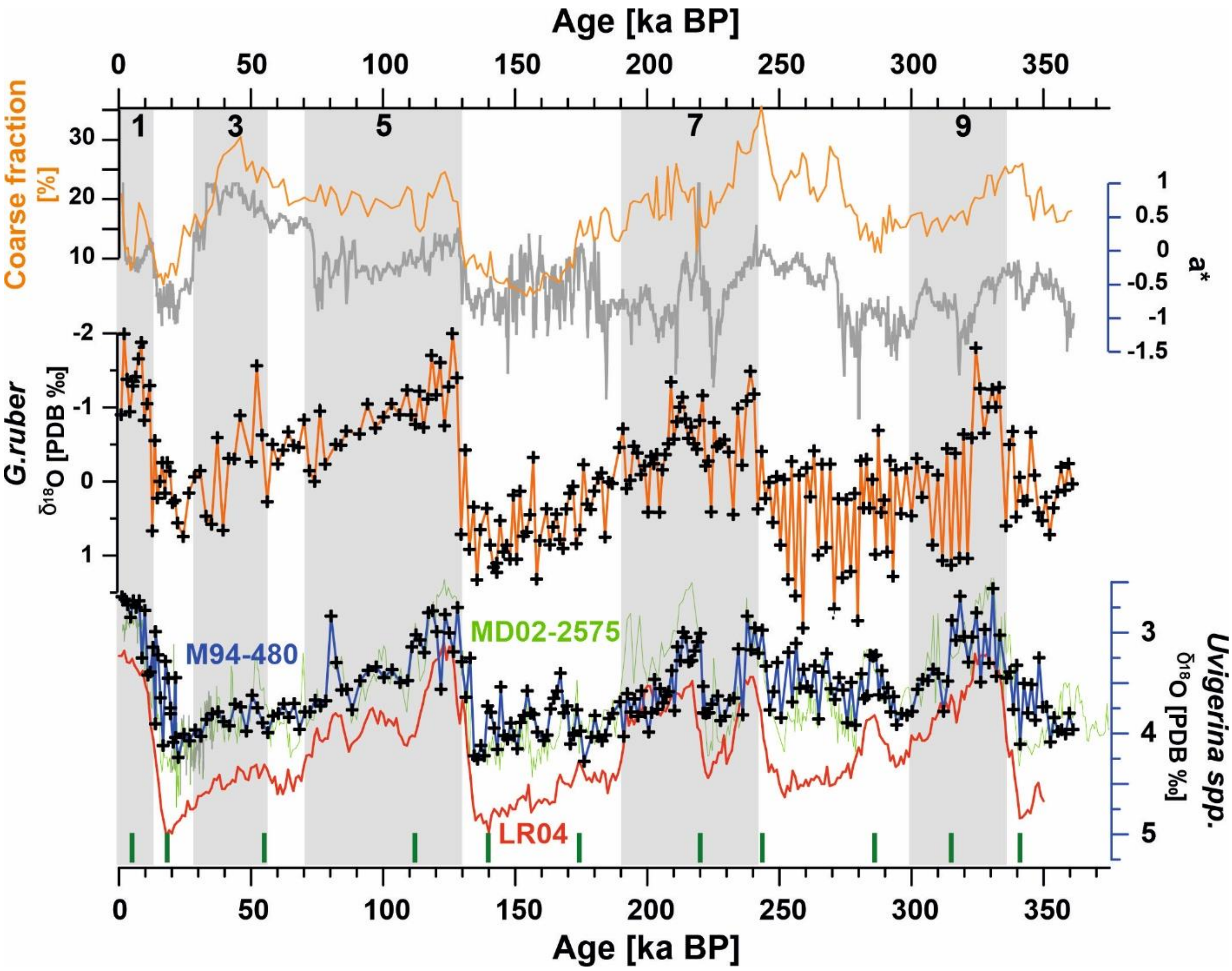

Fig. 9. Chronostratigraphy of core M94-480 PC from Yucatan Strait, 23°48.141N 87°0.868W, 730 m water depth. Bottom: Benthic stable oxygen isotope record ($\delta^{18}O$ in ‰ VPDB) over the last ~360 kyr. The stratigraphic framework is based on tuning the benthic $\delta^{18}O_{U.peregrina}$ record to the global benthic reference stack LR04 (Lisiecki and Raymo, 2005). Green vertical lines mark tie lines between both records. Further support of the age model comes from the tight match to the benthic $\delta^{18}O_{U.peregrina}$ record of core MD02-2575 from the northern Gulf of Mexico, for which a strong response to cyclic fluctuations in Earth's precession and obliquity was proven (Nürnberg et al., 2008). Middle: Planktonic $\delta^{18}O_{G.ruber}$ record (in ‰ VPDB) of core M84-480 PC. Top: Coarse grain fraction (>63 µm*) and high resolution a*-record of core M94-480 reflecting the relationship between green and magenta, which is used to establish the age model for adjacent core M94-482 PC. Interglacial periods are shaded and marine oxygen isotope stages (MIS) are indicated by black numbers.*

In order to extract potential age information from these marine carbonates the strontium isotope stratigraphy (SIS) approach according to Howarth and McArthur (2004) and the given data base therein is applied. Table 1 provides the transfer of $^{87}Sr/^{86}Sr$ ratios into mean SIS ages and of their uncertainties into asymmetric age ranges. The latter are unfortunately large for the context of this study due to the shallow slope of marine Sr isotope evolution in the related time interval.

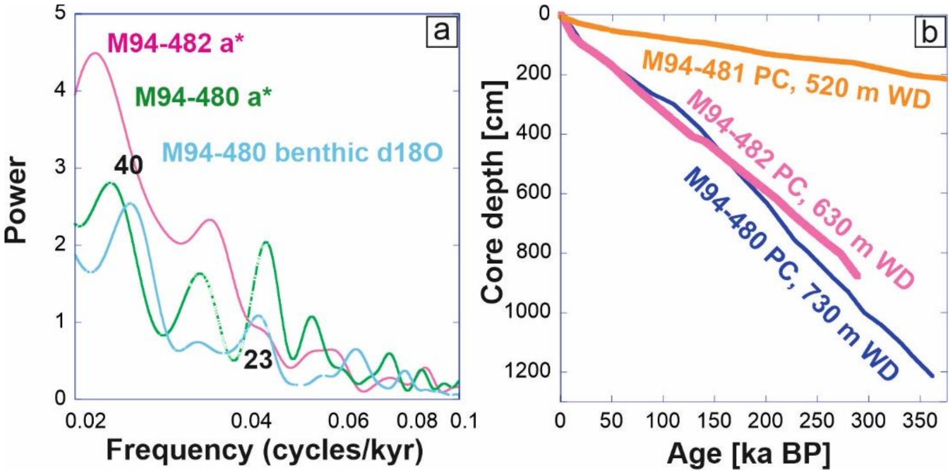

Fig. 10. (a) The B-Tukey frequency spectra of the different proxy data point to orbital forcing. Most pronounced cyclicities of 40 kyr and 23 kyr as a response to cyclic fluctuations in the Earth's orbital parameters obliquity and precession occur in the benthic $\delta^{18}O_{U.peregrina}$ record (light blue). The frequency spectra of color a variations in cores M94-480 PC (green) and M94-482 PC (orange) are less distinct due to the blurry character of the color records. (b) Depth/age diagrams for cores M94-480 PC (blue), -481 PC (orange), and -482 PC (pink) revealing decreasing sedimentation rates with decreasing water depths on the western slope of Yucatan Strait.*

From the determined $^{87}Sr/^{86}Sr$ ratios, a maximum age of 0.83 Ma is implied for the hiatus and the related MPU as observed in the seismic imagery. The residual structure of this enclosed carbonate sediment matrix is dating the shielding brachiopod to be syn- to post-hiatus emplaced. Therefore, its SIS systematic indicates a maximum age of 0.57 Ma for the re-occurrence of a depositional regime and its sediment record investigated in this study. Consequently, this age represents also the set point for estimates of the minimum duration of the hiatus (0.83-0.57 Ma), which falls into the MPT.

4.3.2 Oxygen isotope stratigraphy and core correlation of sediment color data

The chronostratigraphy of core M94-480 PC is based on the graphic correlation of the benthic $\delta^{18}O$ curve (*Uvigerina* spp.) with the stacked $\delta^{18}O$ reference record (LR04) of

Lisiecki and Raymo (2005) using the software AnalySeries (Paillard et al., 1996; Fig. 9). Twelve tie lines were used to tie the benthic $\delta^{18}O$ record to the reference record. The correlation between LR04 and M94-480 PC is high (r^2 = 0.7) and supports the established chronology. High benthic $\delta^{18}O$ values commonly refer to glacial conditions. The marine oxygen isotope stages (MIS) were identified following the standard $\delta^{18}O$ nomenclature proposed by Prell et al. (1986) and Tiedemann et al. (1994).

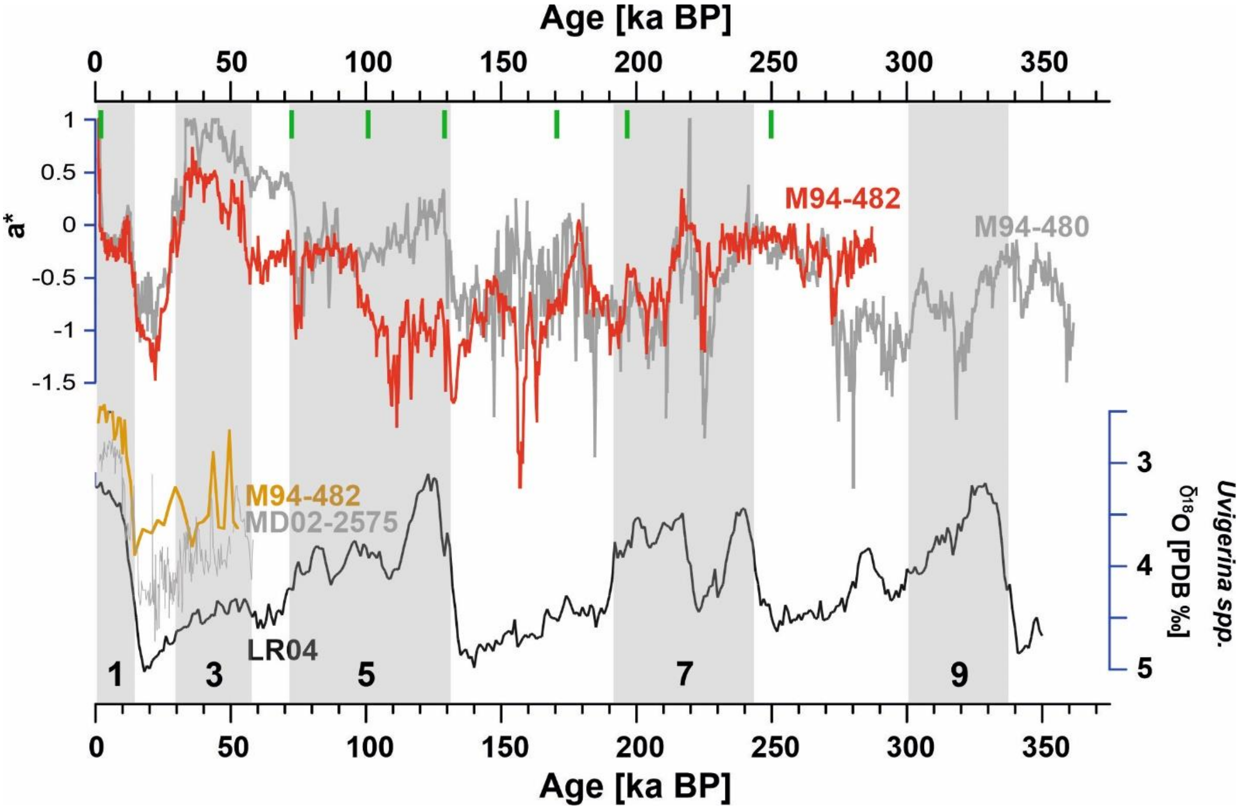

Fig. 11. Chronostratigraphy of core M94-482 from Yucatan Strait, 23°49.155N 87°7.752 W, 630 m water depth. Top: Visual correlation of the a-record (red) to the a*-record of core M94-480 (gray), which serves as stratigraphically classified reference record (c.f. Fig. 9). Green vertical lines mark tie-lines between the records. Bottom: Further support of the age model in the youngest section comes from the correlation of the benthic $\delta^{18}O_{U.peregrina}$ record (orange) to reference sites MD02-2575 from the northern Gulf of Mexico (Nürnberg et al., 2008; gray) and LR04 (Lisiecki and Raymo, 2005; black).*

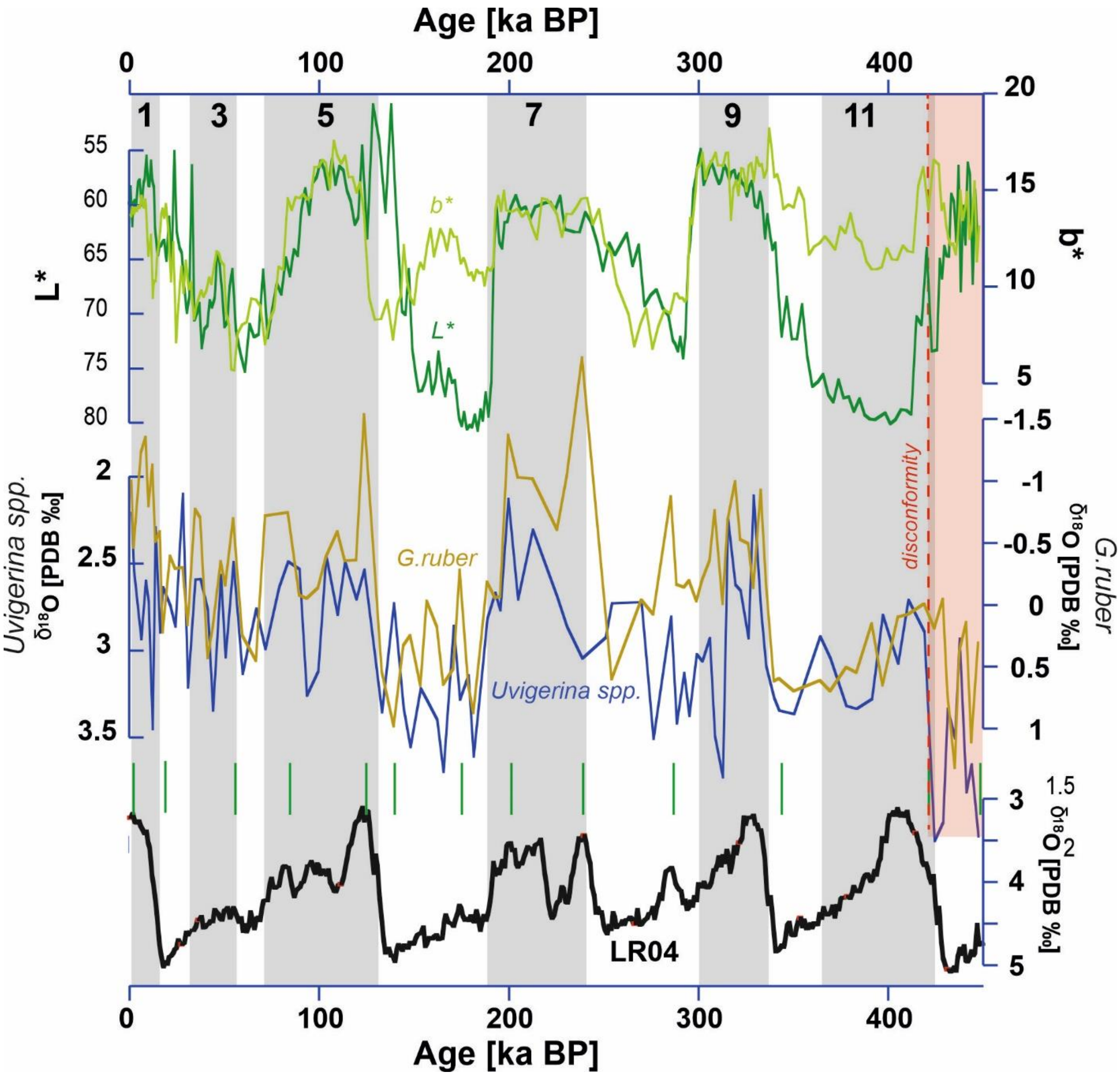

Fig. 12. Chronostratigraphy of core M94-481 from Yucatan Strait, 23°39.997N 87°7.284W, 521 m water depth. Bottom: Global benthic $\delta^{18}O$ reference stack LR04 (Lisiecki and Raymo, 2005; black). Middle: The stratigraphic framework is based on tuning the planktonic $\delta^{18}O_{G.ruber}$ record (in ‰ VPDB; orange) of core M84-481 to the global benthic $\delta^{18}O$ reference stack LR04. Green vertical lines mark tie lines between the records. The correlation is largely supported by the benthic $\delta^{18}O_{U.peregrina}$ record of core M84-481 (blue). Top: L and b*-records of core M84-481 reflecting glacial/interglacial changes from MIS1 to MIS11. A prominent disconformity is dated to ~425ka BP (red dashed line). Below, the strongly lithified coarse-grained sediment contains large brachiopod shells dated with $^{87}Sr/^{86}Sr$.*

The stratigraphical framework of core M94-480 PC covers the last ~360 kyrs, showing typical glacial/interglacial $\delta^{18}O$ variability and amplitudes in both the benthic and the planktonic (*G. ruber*) isotope records. The benthic $\delta^{18}O$ record is further congruent to the benthic $\delta^{18}O$ record of core MD02-2575 from the northern Gulf of Mexico (Nürnberg et al., 2008), for which a strong response to cyclic fluctuations in Earth's orbital parameters was proven (Nürnberg et al., 2008). Similarly, the B-Tukey frequency spectrum of the core M94-480 benthic $\delta^{18}O$ record reveals dominant cyclicities of 40 kyr and 23 kyr as a response to cyclic fluctuations in the Earth's orbital parameters obliquity and precession (Fig. 10).

The glacial/interglacial pattern is not such obvious in the a*-record of core M94-480 (Fig. 9), and the cyclicities of 40 kyr and 23 kyr are notable but not concise (Fig. 10). Nonetheless, the a*-record of core M94-480 is useful to establish a tight correlation to core M94-482 PC.

For core M94-482 PC, we mainly used the highly variable a*-record as age constraint, as it is rather similar to the a*-record of the stratigraphically well-classified core M94-480 PC. The visual correlation of both records afforded 7 tie-lines and resulted in a correlation with r^2 = 0.5 (Fig. 11). Low a*-values mostly but not consistently relate to glacial time periods. Benthic $\delta^{18}O$ across the uppermost 1.8 m of core M94-482 revealing a typical glacial/interglacial $\delta^{18}O$ amplitude were visually correlated to the LR04 (Lisiecki and Raymo, 2005) and MD02-2575 (Nürnberg et al., 2008) reference records (Fig. 11), further supporting the established core chronology.

The stratigraphical range of core M94-482 covers the last ~288 kyrs, showing glacial/interglacial variability in the sedimentary pattern. Due to the blurry character of the core M94-482 a*-record, the B-Tukey spectrum is not clear, although spectral maxima are close to 40 kyr and 23 kyr cyclicities (Fig. 10).

For core M94-481 PC, the stratigraphic interpretation of the foraminiferal $\delta^{18}O$ signal is challenging, because foraminifers are generally rare and partly absent in some core intervals. Also, the $\delta^{18}O$ signals and amplitudes in planktonic and benthic foraminifers do not vary consistently. We visually tuned the $\delta^{18}O_{G.ruber}$ record of core M94-481 to the LR04 $\delta^{18}O$ reference stack of Lisiecki and Raymo (2005), thereby applying 13 tie-lines and receiving a correlation of r^2 = 0.6. Light foraminiferal $\delta^{18}O$ values are consistently related to interglacial time periods. According to the resulting age model, the M94-481 core covers glacial/interglacial changes from MIS1 to 11, with the prominent disconformity at 2.3 m core depth achieving an age of ~425 ka BP. This is consistent to the $^{87}Sr/^{86}Sr$ age estimate of maximum 570 ka BP for a brachiopod shell from right below the disconformity.

The age-depth relationships for cores M94-480 PC and -482 PC appear continuous and without significant disturbances. The average sedimentation rate is ~3$\pm$1 cm/kyr, being slightly higher in the deeper core M94-480 PC. Considerably lower sedimentation rates of 0.6$\pm$0.3 cm/kyr are reconstructed for core M94-481 PC. This is the shallowest and shortest core, but reaches farthest back in time.

4.3.3 Core-seismic integration

The age of the MPU/C can in principle be estimated by extrapolation of the previously determined sedimentation rates, provided that the age-depth function can be applied to the Parasound data. However, the rounded sound velocity of water (1500 m/s) usually used in all profile figures cannot simply be transferred to the sediment cores for accurate extrapolation. For the integration of stratigraphical core and Parasound information, we assume that the relative changes in the coarse (grain) fraction in sediment core M94-480 PC cause the acoustic impedance contrasts. The coarse fraction >63 µm from core M94-480 PC was determined approximately every 5 centimeters (top Fig. 9). Each value was then assigned an age, based on the chronostratigraphy established in Fig. 9 (c.f. Fig. 10b). In order to constrain the correlation between relative seismic reflection amplitudes with assumed acoustic impedance changes, the vertical gradient of the coarse fraction was further determined by calculating the difference between adjacent samples.

In Fig. 13a, the coarse fraction gradient is plotted against time and the LR04 $\delta^{18}O$ reference record. For further consideration, it is unimportant whether the gradient is positive or negative, since the phase information of the Parasound data was not recorded. Because absolute values are not required for neither the coarse fraction gradient nor for $\delta^{18}O$ values both sets of numbers were normalized.

The further procedure assumes that the coarse fraction represents a proxy for the sediment density. In this case, the gradient of the coarse fraction is a proxy for the reflection coefficient. The higher the gradient, the higher the reflection coefficient. Consequently, the coarse fraction gradient should correlate with the reflection amplitudes in the Parasound data. Next, the age-depth function was converted into an age-twt function with various sound velocities. Since no further constrains were available, the simple assumption of a constant velocity seemed to be the most reasonable approach.

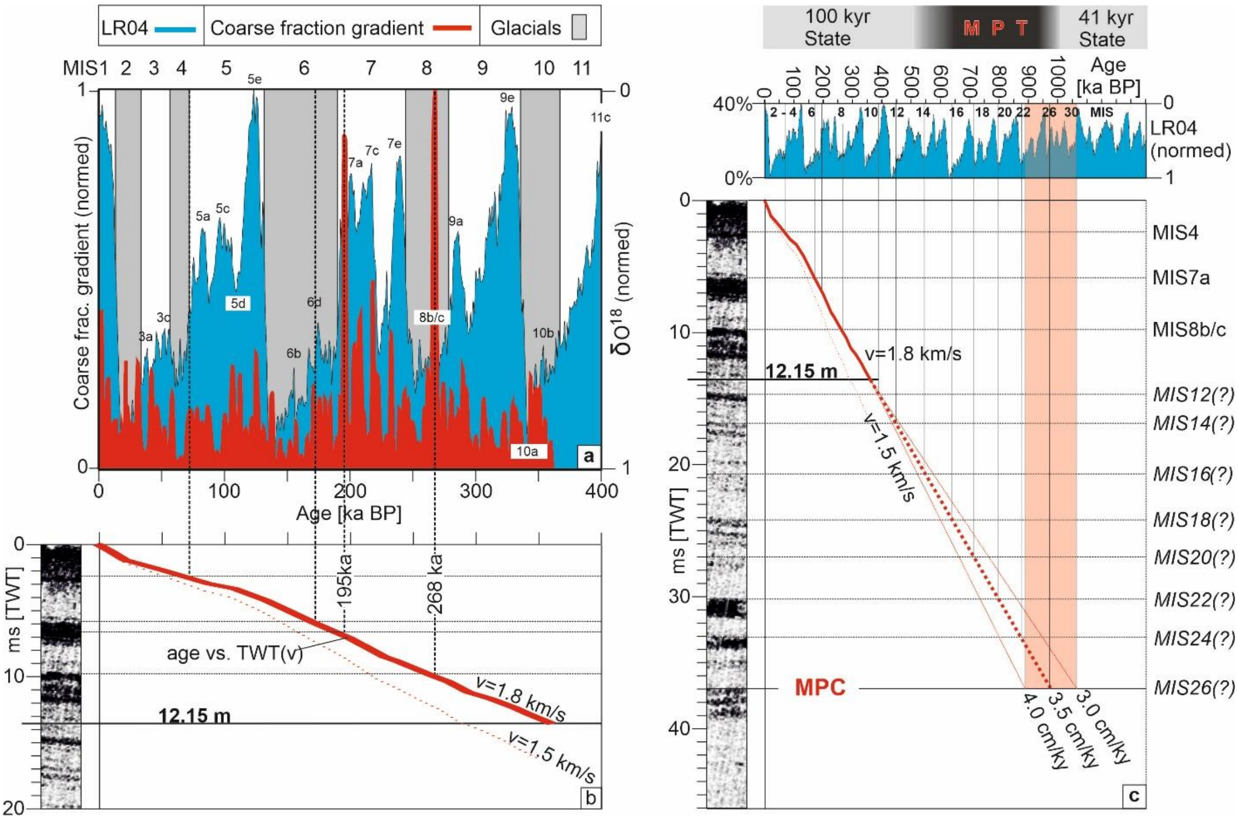

Fig. 13: (a) In the upper figure, the normalized gradient of the coarse fraction of sediment core M94-480 PC (Fig. 9) and the normalized LR04 δ¹⁸O reference record (Lisiecki and Raymo, 2005) are plotted vs. time and MIS. Odd MIS are indicated by grey background color. MIS substages after Railsback *et al. (2015). In the lower figure, reflection amplitudes are correlated with these data. The conversion from age-to-depth (Fig. 10b) to age-to-TWT was performed with a constant sound of 1800 m/s. (b) Extrapolation of age-TWT function yields an age of the MPC between ~900 and 1050 ka BP. See text for discussion.*

When choosing a sound velocity of 1800 m/s, the top of the high amplitude reflection at 6 ms and that at 10 ms TWT correlate quite well with the coarse fraction gradient at MIS 4-5a, 6d, 7a and 8b/c (Fig. 13 a). Depth-conversion with 1800 m/s yields a maximum age of ca. 360 kyrs for the base of the core, which is congruent to the age that was estimated from the stratigraphic analysis of M94-480 PC (Fig. 9).

For the extrapolation of the core data down to the MPU/C we used sedimentation rates between 3 and 4 cm/kyr, because the sedimentation rate for the last 50,000 years in the lower core range (361-314 kyr) varied between these rates (Fig. 13b). As can be seen in Fig. 9, the coarse grain fraction is larger during the sea level highstands (interglacials) than during the lows (glacials). The number of changes between weakly and more reflective time intervals in the Parasound data roughly corresponds to the number of glacial/interglacial changes.

5. Interpretation and Discussion

5.1 Overall setting

Generally, seaward concave, arcuate isobaths in the upslope domain in conjunction with convex isobaths further downslope are typical of headwalls or head scarps of mass transport complexes (MTC; e.g., Bull et al., 2009, and references there in). As there is much evidence that the Chicxulub impact on the northwestern Campeche Bank, western Florida shelf, and Texas coast resulted in large-scale mass remobilization (Paull et al. 2014; Sanford et al., 2016, Pag 2017; 2022; Guzmán-Hidalgo et al., 2021), we suggest that the eastward concave, arcuate 100 m – 300 m isobaths represent the headwall domain of an about 150 km broad MTC (Fig. 1b). Consequently, the lobe shaped 600 m – 1000 m characterizes the top surface of the toe domain. Without any further seismic reflection data we unfortunately cannot rule out that the 100–300 m isobath represents the edge of, e.g., a back-stepping carbonate platform or rim reef.

The convex shaped deposits downslope of the headwall and on top of the MTC can be considered as an infilling or plastered drift (Faugéres and Stow, 2008; Rebesco et al., 2014), which Hübscher et al. (2010) already postulated for the western Florida Shelf. In addition, there is some local evidence for gas escape structures (surface and buried pockmarks; Fig. 4). Pockmarks in shallow deposits of carbonate platforms are generally rare, because the organic carbon content is always very low (Betzler et al., 2011, and references there in). If the pockmark result from expelling hydrocarbon fluids, the source rock should be below the carbonate platform, because any organic carbon content of the Campeche carbonate banks is not reported. Land et al. (1995) described circular structures with a hybrid genesis controlled by submarine fresh water discharge and carbonate dissolution along the Florida margin. Whether this offers a possible explanation for the pockmarks at Campeche Bank can only be clarified by geochemical analysis.

5.2 Geological age constrains

The M94-480 PC core-seismic integration implied that at the core site the MPC is about 28 m (calculated from 37 ms TWT and v=1.8 m/s) and consequently 730 m + 28 m = 758 m beneath present day seafloor. Hence, deposition on the MPC started in that depth right before or during the early MPT (900-1050 Ma; MIS 23-24). The correlation between Parasound data, core derived age models and coarse fraction is built on simplified assumptions. Reflection amplitudes may be well related to carbonate lithification or cementation, compaction etc.. Those factors would also influence the sound velocity in the sediments. Therefore, the following discussion builds on the age estimation that the MPC coincides with the early MPT.

The age constraints for M94-481 PC are less consistent. Sr-isotope analysis of M94-481 PC samples (521 m water depth plus max. 2.3 m sediments) implies a maximum age of 0.83 Ma for the top of the condensed section and onset of non-deposition (hiatus). When the deep base level was at shallower depth than the core site since MIS15, sedimentation commenced. However, because of the insufficient vertical mapping of the MPC in the Parasound data, the exact assignment of the condensed layer to the MPC is unclear at this position and water depth.

5.3 Geophysical age constrains (upper slope)

A seismo-stratigraphic interpretation of Parasound profiles 6 and 7 further constrains the age of upper slope deposits. In profile 6 (Fig. 6), deposits above the MPU and in water depths of 500 m - 600 m can be divided into 15 alternating sequences, one of which alternately terminates against the MPU, and the one above it onlaps against the lower unit. Since the uppermost or youngest unit terminates against the MPU, this can be considered characteristic of highstand deposition. This interpretation would be consistent with the highstand shedding model (Schlager et al., 1994) and a relatively shallower base-level as a result of relative sea level. If the base-level drops during glacial and relative sea level lows, the depositional space shifts downslope. If this assignment of sedimentary units to glacial/interglacial cycles is correct, seven highstand units and six lowstand units can be identified (Fig. 6c, d). Consistently, the unit directly overlying the MPU would be assigned to MIS 15 and the MPU would be assigned to MIS 16. This corresponds to the Sr isotope age estimate.

As the uppermost unit of slope-parallel profile 7 (Fig. 7) is characterized by sediment waves, we conclude that these sediment waves are typical of sea level highstand conditions to the Holocene conditions. Up to seven wavy units, presumably dune fields, can be identified above the MPU. When these highstand deposits are assigned to interglacial MIS, it follows that the MPU formed during glacial MIS 16 and is overlain by interglacial MIS15 deposits. Consequently, a thicker than average (ca. 6-7 m) deposit would have been deposited here during MIS2-4. Betzler et al. (2014) observed similar dune fields or sediment waves at the western Great Bahamas Bank, the crests of which strike along the contours. In our study, the sediment waves are only observed locally in strike profile 7, which is why an interpretation as cyclic steps seems not appropriate.

5.4 Deep base level control on MPU/C

We need to address the issue how the transition from unconformity (MPU) to conformity (MPC) took place. Hübscher et al. (2010) explained the MPU in profile 3 (Fig. 3) by an abruptly strengthened bottom flow that eroded concordant layers. As Hübscher et al. (2010) already noted, a short-lived paleoceanographic event during the MPT is not yet documented. There is also no evidence for mass wasting, which could explain the MPU as a basal shear-surface (decollement) of a slump or slide. We hence argue that the onset of sedimentation further downslope is a function of both increasing current velocities and deep base level. The slightly decreasing sedimentation rates upslope can be explained by the faster surface currents and stronger erosional/winnowing processes.

As summarized e.g. by Chen et al. (2019), strong deep-water bottom currents are often related to THC- or wind-driven currents (e.g., Rebesco, 2005), benthic storms (e.g., Gardner et al., 2017), intermittent mesoscale eddies (e.g., Liang and Thurnherr, 2011; Serra et al., 2010; Rubino et al., 2012; Thran et al., 2018; Chen et al., 2019), and internal waves (Reiche et al., 2016; Quayyum et al., 2017; Miramontes et al., 2020).

In the Yucatan Channel, the highest current velocities are in the central part of the Yucatan Current and decrease towards the slopes of the Yucatan peninsula and Cuba (Sheinbaum et al., 2002). Hübscher et al. (2010) previously showed that in the Yucatan Strait, hydroacoustically detectable sediments do not occur until below 550-600 m. Since the LC continues northwards, it is likely that the LC and episodically separating warm-core rings (eddies) generally control deposition and non-deposition along the eastern Campeche Bank. The internal waves at the TACW/AAIW-boundary and in water depth of ~520-540 m as postulated by Hebbeln et al. (2014) control the deep base level itself, as significant sedimentation currently only occurs below this depth. According to this rather conceptual explanation, the presence of internal waves is not crucial, since the deep base level can simply be explained by a decrease of the flow velocity of the LC. Eddies and benthic storms tend to be episodic events, however, on geologic time scales they can be considered quasi-continuous processes. In this regard, deep eddies generally act in water depths >1000 m (Oey, 2008) and can thus be ruled out as causative for deep base level. The same applies to mesoscale eddies as described, e.g., by Chen et al. (2019), which also affect continental slopes in water depth of >1000 m.

5.5 Deep base level fluctuations

The duration of the deep base level fall that caused the forced regression systems tract-like offlapping clinoforms beneath the MPU is unconstrained. Since the supra-MPU/C strata comprise several glacial/interglacial cycles, a single eustatic sea level fall cannot be accounted for the deep base level fall by more than 100 m, since the offlapping strata were deposited during the deep base level fall. Further, this offlapping sediment package of the toplapping clinoforms beneath the MPU is much thicker than the several 100 kyrs old overburden of the MPU/C. Hence, the offlapping sediment package comprises at least several 100 kyrs as well (Figs. 6c, 8c). In contrast to hydrodynamic explanations, a deep base level fall or rise can theoretically also be explained by subsidence or tectonically controlled uplift. However, as no such studies exist, a tectonic control of the here described processes can be ruled out.

It is reasonable to assume that the deep base level fall resulted from the LC intensification during the narrowing and closure of the Panama Isthmus in the middle or late Pliocene. The truncation of prograding clinoforms above 400 m water depth and the lack of sedimentation since then (Fig. 8) can also be interpreted by the onset of the LC or its amplification.

The continuously upslope shifting onlap termination of the supra MPU-strata at the upper slope (Figs. 6a, 8a) imply a deep base level rise. This is consistent with the age models discussed previously, which dated the MPC to the beginning of the MPT, and the sediments above the MPU on the upper slope to the outgoing MPT or to the time after. Similar to the Levant margin (eastern Mediterranean), the deep base level rise created a sigmoidal sediment body that reveals characteristics comparable to Transgressive Systems Tracts (Hübscher et al., 2016). That the sedimentary package above the

MPU/C generally terminates as onlap against the MPU, but was deposited during the post MPC glacial-interglacial cycles, provides evidence of an overall weakening of the flow regime along the upper slope of the eastern Campeche Bank since the MPT. The weakening of the flow regime created the accommodation space above the MPU.

The uniformity of supra-MPU/C deposition suggests that the cause is not a gradual decline in the shedding of more local and episodic eddies, but a weakening of the contour-parallel LC. This attenuation holds on average for all other fluctuations, e.g., pycnocline disappearance during glacials (Matos et al. 2017), shedding of anticyclonic eddies (e.g., Oey, 2008; Nürnberg et al., 2008; Nürnberg et al., 2015), but also seasonal variations (Wiseman and Dinnel, 1988; Sheinbaum et al., 2002).

5.6 Paleoceanography and Paleoclimate implications

5.6.1 MPT

According to the core-seismic integration, the maximum depth of the deep base level was reached at ca. 950-1100 kyr BP, i.e., at the onset of the MPT. If the deep base level correlates with the water transport and associated heat transfer from the western Atlantic warm water pool towards the North Atlantic via the AMOC, the mid-Pleistocene heat transport was maximum then. Subsequently, the deep base level shifted upward, implying a reduced current-related heat transfer. A close link between LC strength and ocean THC is likely, as the onset of the deep base level (~950 ka BP) is consistent with a major disruption of the THC system during the MPT between MIS 25 and 21 at ~950 to 860 ka BP (Pena and Goldstein, 2014; Kim et al., 2021).

The uplift of the deep base level documents the overall weakening of the LC and thus a reduction in heat transport from the Caribbean to the North Atlantic via Florida Straits, which is consistent with these notions. As summarized by Pena and Goldstein (2014), several authors explained the MPT by cooling of sea-surface temperatures and increased high-latitude sea-ice expansion (Gildor and Tziperman, 2010; Martinez-Garzia et al., 2010; McClymont et al., 2013) and/or changes in THC vigor (Raymo et al., 1990).

5.6.2 The post-MPT 100.000 yr world

The seismic imagery of our study further shows that the reflection pattern above the MPU/C and in water depths above ~660-680 m changes from slightly wavy to sub-parallel to parallel, i.e., becoming more and more straight in the upmost layers (Figs. 3-

5). Averaged over astronomical cycles, this argues for a steady decrease in LC vigor. The dependency of LC vigor and the net through flow via the Yucatan and Florida straits on glacial/interglacial periods, however, remains a matter of debate.

As the highstand dune fields (Fig. 7) indicate a higher-energy depositional environment than the parallel layers between them, the proposed age model in Fig. 7 implies weaker bottom currents during glacials (sea level low-stands) than during the interglacials (high-stands). Stieglitz et al. (2009; 2011) argued for a reduced Florida Straits transport during the LGM and Younger Dryas. Based on the Nd-proxy analysis, Pena and Goldstein (2014) and Kim et al. (2021) also concluded on the reduction of AMOC vigor during the glacials. However, the latter observation can also be explained by the fact that a large part of the northward AMOC transport during the lows does not pass through the Yucatan Strait, but takes place east of the Caribbean Islands (Antilles, etc.). Brunner (1984) explained higher sand contents (preferentially foraminiferal tests) in warm climate sediments from the Yucatan Channel by lowered sedimentation rates due to stronger winnowing of the fine grain fraction. The positive correlation between the coarse grain fraction of M94-480 PC and sea level (cf. Fig. 13) can be interpreted in the same way. However, this interpretation is not unambiguous, because the increased relative proportion of the coarse grain fraction consisting mainly of foraminifera-during sea level highstands can also be explained by increased marine productivity.

In contrast, the eddy-permitting model simulations of Nürnberg et al. (2015) imply that the southward shift of the Intertropical Convergence Zone and the strengthened atmospheric circulation during glacial periods intensified the (wind-driven) Sverdrup transport within the Subtropical Gyre (Slowey and Curry, 1995). At the same time, the lowered sea level and the related smaller Yucatan Strait cross section rather caused the strengthening of the Yucatan and Florida straits throughflow. In response to the stronger throughflow, the LC eddy shedding in the Gulf of Mexico vanished, which would explain the extreme sea surface cooling in the northern Gulf (Nürnberg et al., 2008; 2015).

The different notions on either glacially reduced or intensified LC flow cannot be conclusively answered yet. Under the following assumptions, the flow velocity of the LC must have been lower during the glacial than during the interglacial periods: If the reflection patterns in Fig. 7 are interpreted correctly in terms of inferred flow velocity, sealevel and climate change, if this local observation is representative of the entire eastern Campeche Bank, and if the coarse grain fraction in sediment cores is a result of winnowing,

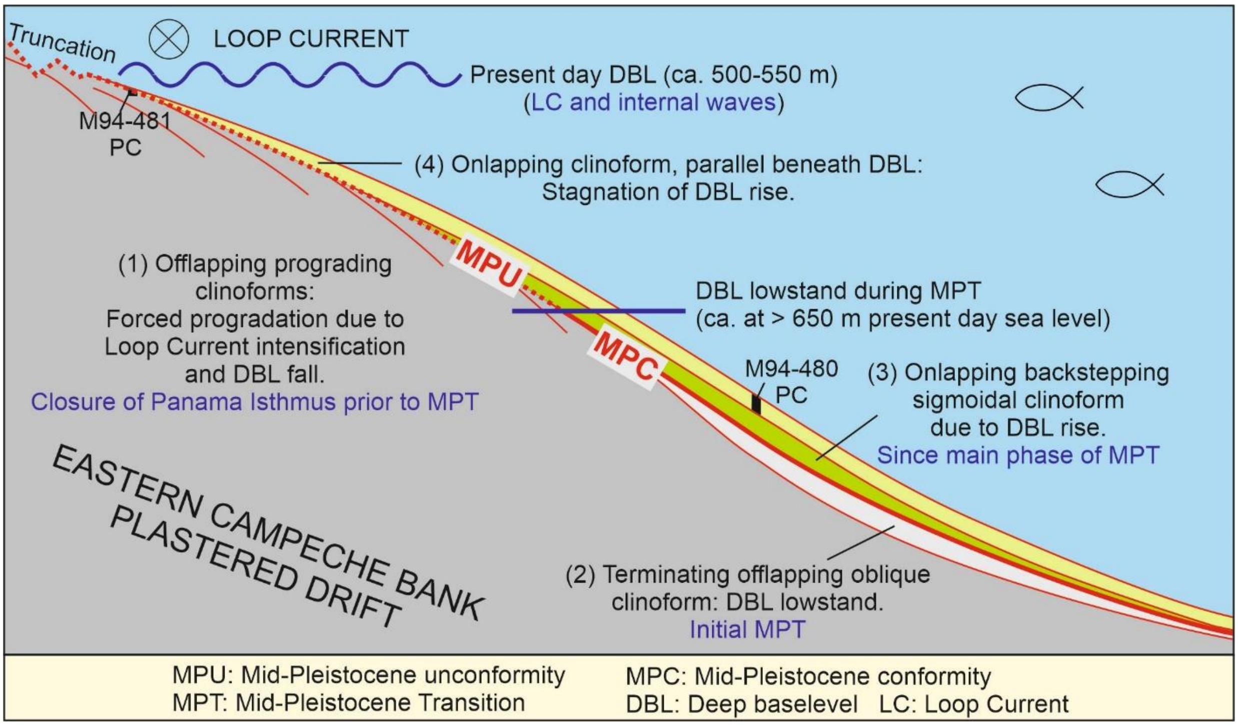

Fig. 14: Summary sketch, manly based on profile 8 across the central drift (Fig. 8).

6. Conclusions

Similar to the northern margin of Campeche Bank, the bathymetry of the eastern Campeche Bank between 22° and 23.5° north and in water depths between 100 m and 1000 m indicates that over a distance of about 150 km the upper slope was remobilized. Since the Chicxulub impact could be shown to be the cause for similar mass failures at the northern margin of Campeche Bank, it can be speculated that the impact was also the cause here.

The deposition processes are summarized conceptually in Fig. 14. Approximately between 500 and 650 m present day water depth, the Parasound data depict prograding and offlapping clinoforms about 20-30 m below the seafloor that are similar to a forced regression systems tract well known from continental shelves. The downslope bounding clinoform is oblique. While on continental shelves the relative sea level under additional influence from the storm wave base or tides control the base level, the deep base level fall here can be interpreted by LC amplifying until the initial MPT. The deep base level fall led to erosion and truncation of prograding deposits above 500 m. No sedimentation during MPT until MIS15 created a hiatus and condensed section at the upper slope.

The offlaps form an unconformity (MPU) that is concordantly overlain. This sigmoidal sediment sequence above resembles a transgressive systems tract. The overlying sedimentary sequence retrogrades and onlaps the MPU. Below 650 m, the MPU becomes its correlated conformity (MPC). In each case, the youngest seismically resolved onlap is at about 500-550 m. This 20-30 m thick sigmoidal sedimentary sequence above the MPU/C represents a plastered drift.

The transition from deep base level fall prior to the MPT to deep base level rise documents a weakening of the LC initially during the MPT. After the MPT, the LC continues to weaken, most prominent during glacials. Since this implies a reduction of the heat transport from the western Atlantic warm water pool into the North Atlantic and consequently up to NW Europe, the general weakening of the LC may explain the further cooling of the Northern hemisphere after the MPT.

Funding

RV METEOR expedition M94 was funded by the German Research Foundation (DFG) and the Federal Ministry of Education and Research (BMBF).

Declaration of competing interests

The authors declare that they have no known competing financial interests or personal relationships that could have appeared to influence the work reported in this paper.

Data statement

Sediment core (Nürnberg, 2022a-f), Parasound (Hübscher, 2022a) and multibeam (Hübscher, 2022b) data will be available from PANGAEA data base oncee the manuscript will be accepted by the journal.

Acknowledgements

We thank Volker Liebtreu for the strontium dating. Volker unfortunately passed away before the publication of this study. We further thank two anonymous reviewers who helped improve the manuscript. We like to thank captain Michael Schneider, his officers and crew of RV METEOR for their support of our measurement programme. We further like to thank Wolfgang Mahrle (German Federal Foreign Office) and

Hubertus von Römer (German Embassy Mexico City) for their great support during the diplomatic clearance for expedition M94.

Figure Captions

Fig. 1: Chronology of the Mid-Pleistocene climate transition (after Schmieder et al. 2000). Shift in mean and lagged onset of 100 kyr cyclicity of global ice volume (a) reflected in the stacked $\delta^{18}O$ global reference record (Lisiecki and Raymo, 2005) and (b) schematic view of the Mid-Pleistocene Climate Transition schematized after Mudelsee and Schulz (1997).

*Fig. 2: (a) Bathymetric map of southern Gulf of Mexico with adjacent Yucatan and Florida straits. The red lines indicate the simplified Loop Current during different seasons. Thin white line indicates M94 track (Hübscher et al., 2013). CIC = Chicxulub impact crater (*Paull et al., 2014). *(b) M94 cruise track (white lines), core sites (star symbols) and seismic profiles 3-8 (yellow lines), which correspond to the figures 3-8. Isobaths are plotted at 100 m intervals. PC = piston core; PS = Parasound. Bathymetric dataset: ETOPO1 (Amante et al., 2009).*

Fig. 3: (a) Parasound profile 3 collected during RV Meteor expedition M78/1 (Hübscher and Pulm, 2009) from eastern Campeche Bank (Hübscher et al., 2010) with location of piston core M94-482 PC. Core length has been calculated with a sound velocity of 1.5 m/ms, which might be too low (see chapter 5 for discussion). (b) Bathymetric map of study area (see also Fig. 2b) (c) Flattened profile of lower eastern Campeche Bank slope (for explanation see Chapter 3). CWC = Cold-water coral; MPU = Mid-Pleistocene Unconformity; MPC = Mid-Pleistocene Correlated Conformity (MPC); VE = vertical exaggeration.

Fig. 4: (a) Parasound profile 4 (thick black line in b) with red line marking the Mid-Pleistocene Unconformity (MPU), which transforms into the correlated conformity (MPC). Piston core locations M94-480 PC and -481 PC and penetration depth are indicated. A black arrow marks the cross-point with profile 5 at site M94-480 PC. Core length calculated with 1.8 m/ms (see chapter 5 for discussion). For location see (b). (c) Flattened Parasound profile in detail. Blue arrows mark pockmarks. Note that the up-warping of the reflections at the north-eastern end of the flattened profile results from the truncation at the head scarp only. (d) Multi-beam (SIMRAD EM122) data showing pockmarks and moat along the head scarp. VE = vertical exaggeration.

Fig. 5: (a) Parasound profile 5 and (b) according line drawing. Red line in (b) marks Mid-Pleistocene Unconformity and correlated conformity (MPU/C). PC480 labels piston core M94-480 PC, which is also the cross-point (black arrow) with the Parasound profile 4. Core length calculated with 1.8 m/ms (see chapter 5 for discussion). The cross-point with the Parasound profile 6 (black arrow to the right) is at the southeastern end of the profile. Note the southeastward amplitude decrease (ad) of reflections beneath ~12 m in the middle of the profile. VE = vertical exaggeration.

Fig. 6: (a) Parasound profile 6 running perpendicular to the continental slope. For location see insert map (b). Red line = Mid-Pleistocene Unconformity (MPU) and Correlated Conformity (MPC). Black arrow = cross-point with profile 5. (c) Flattened profile. Red arrows = onlaps and downlaps. (d) Line drawing with interpreted sea level highstand (dark blue), lowstand deposits (light blue) and suggested correlation with MIS. (e) Enlargement from upper slope. VE = vertical exaggeration.

Fig. 7: (a) Parasound profile 7 almost parallel to the contour. (b) The profile 7 is too short to be resolved in the insert map. It runs almost parallel to the slope. The black triangle marks, where the profile stops at profile 8. Red line = Mid-Pleistocene Unconformity (MPU). Red arrows = wavy horizons and suggested correlation with MIS. VE = vertical exaggeration.

Fig. 8: (a) Parasound profile 8. Red line = Mid-Pleistocene Unconformity (MPU) and Correlated Conformity (MPC). Black arrow = cross-point with profile 7. For location see insert map (b). (c) Flattened profile with red arrows marking toplap terminations. The signal to noise ratio of internal reflection amplitudes is rather small. In order to identify reflection terminations and to distinguish between the MPU and the MPC, the grey scale colors are inverted. (d) Upslope prolongation of (a). Note the sea floor "pulse-train" multiple (see chapter 3.2 for explanation) and the different vertical exaggeration (VE) compared to (a).

Fig. 9. Chronostratigraphy of core M94-480 PC from Yucatan Strait, 23°48.141N 87°0.868W, 730 m water depth. Bottom: Benthic stable oxygen isotope record ($\delta^{18}O$ in

‰ VPDB) over the last ~360 kyr. The stratigraphic framework is based on tuning the benthic $\delta^{18}O_{U.peregrina}$ record to the global benthic reference stack LR04 (Lisiecki and Raymo, 2005). Green vertical lines mark tie lines between both records. Further support of the age model comes from the tight match to the benthic $\delta^{18}O_{U.peregrina}$ record of core MD02-2575 from the northern Gulf of Mexico, for which a strong response to cyclic fluctuations in Earth's precession and obliquity was proven (Nürnberg et al., 2008). Middle: Planktonic $\delta^{18}O_{G.ruber}$ record (in ‰ VPDB) of core M84-480 PC. Top: Coarse grain fraction (>63 µm*) and high resolution a*-record of core M94-480 reflecting the relationship between green and magenta, which is used to establish the age model for adjacent core M94-482 PC. Interglacial periods are shaded and marine oxygen isotope stages (MIS) are indicated by black numbers.*

Fig. 10. (a) The B-Tukey frequency spectra of the different proxy data point to orbital forcing. Most pronounced cyclicities of 40 kyr and 23 kyr as a response to cyclic fluctuations in the Earth's orbital parameters obliquity and precession occur in the benthic $\delta^{18}O_{U.peregrina}$ record (light blue). The frequency spectra of color a variations in cores M94-480 PC (green) and M94-482 PC (orange) are less distinct due to the blurry character of the color records. (b) Depth/age diagrams for cores M94-480 PC (blue), -481 PC (orange), and -482 PC (pink) revealing decreasing sedimentation rates with decreasing water depths on the western slope of Yucatan Strait.*

Fig. 11. Chronostratigraphy of core M94-482 from Yucatan Strait, 23°49.155N 87°7.752 W, 630 m water depth. Top: Visual correlation of the a-record (red) to the a*-record of core M94-480 (gray), which serves as stratigraphically classified reference record (c.f. Fig. 9). Green vertical lines mark tie-lines between the records. Bottom: Further support of the age model in the youngest section comes from the correlation of the benthic $\delta^{18}O_{U.peregrina}$ record (orange) to reference sites MD02-2575 from the northern Gulf of Mexico (Nürnberg et al., 2008; gray) and LR04 (Lisiecki and Raymo, 2005; black).*

Fig. 12. Chronostratigraphy of core M94-481 from Yucatan Strait, 23°39.997N 87°7.284W, 521 m water depth. Bottom: Global benthic $\delta^{18}O$ reference stack LR04 (Lisiecki and Raymo, 2005; black). Middle: The stratigraphic framework is based on tuning the planktonic $\delta^{18}O_{G.ruber}$ record (in ‰ VPDB; orange) of core M84-481 to the global benthic $\delta^{18}O$ reference stack LR04. Green vertical lines mark tie lines between

the records. The correlation is largely supported by the benthic $\delta^{18}O_{U.peregrina}$ *record of core M84-481 (blue). Top: L* and b*-records of core M84-481 reflecting glacial/interglacial changes from MIS1 to MIS11. A prominent disconformity is dated to ~425ka BP (red dashed line). Below, the strongly lithified coarse-grained sediment contains large brachiopod shells dated with* $^{87}Sr/^{86}Sr$*.*

Fig. 13: (a) In the upper figure, the normalized gradient of the coarse fraction of sediment core M94-480 PC (Fig. 9) and the normalized LR04 $\delta^{18}O$ *reference record (Lisiecki and Raymo, 2005) are plotted vs. time and MIS. Odd MIS are indicated by grey background color. MIS substages after* Railsback *et al. (2015). In the lower figure, reflection amplitudes are correlated with these data. The conversion from age-to-depth (Fig. 10b) to age-to-TWT was performed with a constant sound of 1800 m/s. (b) Extrapolation of age-TWT function yields an age of the MPC between ~900 and 1050 ka BP. See text for discussion.*

Fig. 14: Summary sketch, manly based on profile 8 across the central drift (Fig. 8).

References

Antoine, J.W., Ewing, J.I., 1963. Seismic refraction measurements on the margins of the Gulf of Mexico. J Geophys Res 68, 1975-1996

Amante, C. and B. W. Eakins, ETOPO1 1 Arc-Minute Global Relief Model: Procedures, Data Sources and Analysis. NOAA Technical Memorandum NESDIS NGDC-24, 19 pp, March 2009. Go to this web site: http://www.ngdc.noaa.gov/mgg/global/global.html.

Balsam W.L., Beeson J.P., 2003. Sea floor sediment distribution in the Gulf of Mexico. Deep-Sea Research I 50, 1421-1444

Betzler, C., Lindhorst, S., Hübscher, C., Lüdmann, T., Fürstenau, J., 2011. Giant pockmarks in a carbonate platform (Maldives, Indian Ocean). Marine Geology, 289, 1-16.

Betzler, C., Lindhorst, S., Eberli, G., Lüdmann , T., Möbius, J., Ludwig, J., Schutter, I., Wunsch, M., Reijmer, J.J.G., Hübscher, C., 2014. Periplatform drift: The combined result of contour current and off-bank transport along carbonate platforms. Geology 42(10), 871-874.

Brunner, C.A. 1984. Evidence for increased volume transport of the Florida Current in the Pliocene and Pleistocene. Marine Geology 54, 223-235

Bull, S., Cartwright, J., & Huuse, M. (2009). A review of kinematic indicators from mass-transport complexes using 3D seismic data. Marine and Petroleum Geology, 26(7), 1132-1151.

Catuneanu, O., Abreu, V., Bhattacharya, J.P., Blum, M.D., Dalrymple, R.W., Eriksson, P.G., Fielding, C.R., Fisher, W.L., Galloway, W.E., Gibling, M.R., Giles, K.A., Holbrook, J.M., Jordan, R., Kendall, C. G. St. C., Macurda, B., Martinsen, O.J., Miall, A.D., Neal, J.E., Nummedal, D., Pomar, L., Posamentier, H.W., Pratt, B.R., Sarg, J.F., Shanley, K.W., Steel, R.J., Strasser, A., Tucker, M.E., Winker, C., 2009. Towards the standardization of sequence stratigraphy. Earth-Science Rev. 92, 1-33.

Emiliani, C., 1975. Paleoclimatological analysis of Late Quaternary cores from the northeastern Gulf of Mexico. Science 189, 1083-1089

Ezer, T., Oey, L.-Y., Lee H.-C., Sturges, W. 2003. The variability of currents in the Yucatan Channel: analysis of results from a numerical ocean model. Journal of Geophysical Research, 108(C1), 3012

Faugères J-C, Stow DAV. 2008. Contourite drifts: nature, evolution and controls. In Contourites, Rebesco M, Camerlenghi A (eds), Developments in Sedimentology 60. Elsevier: Amsterdam; 257–288.

Flower, B.P., Hastings, D.W., Hill, H.W., Quinn, T.M., 2004. Phasing of deglacial warming and laurentide ice sheet melt water in the gulf of Mexico. Geology 32(7), 597–600

Gardner, W.D., Tucholke, B.E., Richardson, M.J., Biscaye, P.E., 2017. Benthic storms, nepheloid layers, and linkage with upper ocean dynamics in the western North Atlantic. Mar. Geol. 385, 304–327.

Gardulski, A.F., Mullins, H.T., Weiterman, S. 1990. Carbonate mineral cycles generated by foraminiferal and pteropod response to Pleistocene climate: West Florida ramp slope. Sedimentology 37, 727-743.

Gardulski, A.F., Marguerite, H.G., Milsark, A., Weiterman, S.D., Sherwood, W.W. Jr., Mullins, H.T., 1991. Evolution of a deep-water carbonate platform: Upper Cretaceous to Pleistocene sedimentary environments on the west Florida margin. Marine Geology, 101, 163-179

Gildor, H., Tziperman, E., 2010. Sea ice as the glacial cycles' climate switch: role of seasonal and orbital forcing. Paleoceanography 15, 605–615

Guzmán-Hidalgo, E., Grajales-Nishimura, J.M., Eberli, G.P., Aguayo-Camargo, J.E., Urrutia-Fucugauchi, J., Pérez-Cruz, L., 2021.

Hebbeln, D., Wienberg, C., Wintersteller, P., Freiwald, A., Becker, M., Beuck, L., Dullo, C., Eberli, G.P., Glogowski, S., Matos, L., Forster, N., Reyes-Bonilla, H., Taviani, M., 2014. Environmental forcing of the Campeche cold-water coral province, southern Gulf of Mexico. Biogeosciences, 11, 1799-1815

Hönisch, B., Hemming, N. G.., Archer, D., Siddall, M., McManus, J. F., 2009. Atmospheric carbon dioxide concentration across the mid-Pleistocene transition. Science 324, 1551–1554.

Howarth, R. J. and McArthur, J. M.: Strontium isotope stratigraphy, in A Geological Time Scale, with Look-up Table Version 4, edited by: Gradstein, F. M. and Ogg, J. G., Cambridge University Press, Cambridge, U.K., 96–105, 2004.

Hübscher, C., 2022a. Sediment echosounder processed data (Atlas Parasound P70 echosounder working area dataset) of RV METEOR during cruise M78/1 & M94, eastern Campeche Bank, Gulf of Mexico. PANGAEA, https://doi.org/10.1594/PANGAEA.950414.

Hübscher, C., 2022b. Multibeam bathymetry processed data (EM 120 echosounder working area dataset) of RV METEOR during cruise M94, eastern Campeche Bank, Gulf of Mexico. PANGAEA, https://doi.org/10.1594/PANGAEA.950412.

Hübscher, C., Pulm, P., 2009. Parasound. In: J. Schönfeld, A. Bahr, B. Bannert, A.-S. Bayer, M. Bayer, C. Beer, T. Blanz, W.-C. Dullo, S. Flögel, T. Garlichs, B. Haley, C. Hübscher, N. Joseph, M. Kucera, J. Langenbacher, D. Nürnberg W.-T. Ochsenhirt, A. Petersen, P. Pulm, J. Titschack, L. Troccoli (2011) Surface and Intermediate Water hydrography, planktonic and benthic biota in the Caribbean Sea – Climate, Bio and Geosphere linkages (OPOKA) - Cruise No. M78/1 - February 22 - March 28, 2009 - Colón (Panama) - Port of Spain (Trinidad and Tobago). METEOR-Berichte, M78/1, 40 pp., DFG-Senatskommission für Ozeanographie, DOI:10.2312/cr_m78_1

Hübscher, C., Dullo, C., Flögel, S., Titschack, J., Schönfeld, J. 2010. Contourite drift evolution and related coral growth in the eastern Gulf of Mexico and its gateways. International Journal of Earth Science, 99(1) 191-206

Hübscher, C., D. Nürnberg, M. Al Hseinat, M. Alvarez García, Z. Erdem, N. Gehre, A. Jentzen, C. Kalvelage, C. Karas, B. Kimmel, T. Mildner, A. O. Ortiz, A. O. Parker, A. Petersen, A. Raeke, S. Reiche, M. Schmidt, B. Weiß, D. Wolf (2014) Yucatan Throughflow - Cruise No. M94 – March 12 – March 26, 2013 – Balboa (Panama) – Kingston (Jamaica). METEOR Berichte, M94, 32 pp., DFG-Senatskommission für Ozeanographie, DOI:10.2312/cr_m94

Hübscher, C., Betzler, C., Reiche, S., 2016. Seismo-stratigraphic evidences for deep base level control on middle to late Pleistocene drift evolution and mass wasting along southern Levant continental slope (Eastern Mediterranean). Journal of Marine and Petroleum Geology 77, 526-534.

Imbrie, J., Berger, A., Boyle, E.A., Clemens, S.C., Duffy, A., Howard, W.R:, Kukla, G., Kutzbach, J., Martinson, D.G., McIntyre, A., Mix, A.C., Molfino, B., Morley, J.J., Peterson, L.C., Pisias, N.G., Prell, W.L., Raymo, M.E., Shackleton, N.J., Toggweiler, J.R., , 1993. On the structure and origin of major glaciation cycles. Part 2: the 100,000-year cycle. Paleoceanography, 8 699-735

Johns, W.E., Townsend, T.L., Fratantoni, D.M., Wilson, W.D., 2002. On the Atlantic inflow to the Caribbean Sea. Deep Sea Research Part 1: Oceanographic Research Papers.

Kaiser, E. A., Caldwell, A., & Billups, K. (2019). North Atlantic upper-ocean hydrography during the mid-Pleistocene transition evidenced by Globorotalia truncatulinoides coiling ratios. Paleoceanography and Paleoclimatology, 34, 658–671. https://doi.org/10.1029/2018PA003502

Kim, J., Goldstein, S.L., Pena, L.D., Jaume-Seguí, M., Knudson, K.P., Yehudai, M., Bolge, L., 2021. North Atlantic Deep Water during Pleistocene interglacials and glacials. Quaternary Science Reviews 269, 107146, https://doi.org/10.1016/j.quascirev.2021.107146

Land, L.A., Paull, C.K., Hobson, B., 1995. Genesis of a submarine sinkhole without subaerial exposure: Straits of Florida. Geology 23(10), 949-951

Liang, X., Thurnherr, A.M., 2011. Subinertial variability in the deep ocean near the East Pacific rise between 9° and 10°N. Geophys. Res. Lett. 38.

Lin, H.L., Peterson, L.C., Overpeck, J.T., Trumbore, S.E., Murray, D.W., 1997. Late Quaternary climate change from δ18O records of multiple species of planktonic foraminifera: high resolution records from the anoxic Cariaco Basin, Venezuela. Paleoceanography 12, 415–427.

Lutze, G. F., Sarnthein, M., Koopmann, B., Pflaumann, U., Erlenkeuser, H. and Thiede, J., 1979. "Meteor" Core 12309: Late Pleistocene reference section for interpretation of the Neogene of Site 397. In: U. yon Rad, W. B. F. Ryan, et al., Init. Rep. Deep Sea Drill. Proj., 47A: 727--739.

Lisiecki, L.E., Raymo, M.E., 2005. A Pliocene–Pleistocene stack of 57 globally distributed benthic δ18O records. Paleoceanography 20, PA1003. doi:10.1029/2004PA001071

Lynch-Stieglitz, J., Curry, W.B., Lund, D.C., 2009. Florida straits density structure and transport over the last 8,000 years. Paleoceanography and Paleoclimatology 24(3). doi.org/10.1029/2008PA001717

Lynch-Stieglitz, J., Schmidt, M.W., Curry, W.B., 2011. Evidence from the Florida Straits for Younger Dryas ocean circulation changes. Paleoceanography and Paleoclimatology 26(1). https://doi.org/10.1029/2010PA002032

Martínez-Garcia, A. Rosell-Melé, A., McClymont, E.L., Gersonde, R., Haug, G.H., 2010. Subpolar Link to the Emergence of the Modern Equatorial Pacific Cold Tongue. Science 328, 1550–1553

Martini, E., 1971. Standard Tertiary and Quaternary calcareous nannoplankton zonation. Proc. Planktonic Conf., 2nd, Roma, 1970, 2: 739--785.

Matos, L., Wienberg, C., Titschack, J., Schmiedl, G., Frank, N., Abrantes, F., Cunha, M.R., Hebbeln, D., 2017- Coral mound development at the Campeche cold-water coral province, southern Gulf of Mexico: Implications of Antarctic Intermediate Water increased influence during interglacials. Marine Geology 392, 53-65.

McClymont, E.L., Sosdian, S.M., Rosell-Melé, A., Rosenthal, Y., 2013. Pleistocene sea-surface temperature evolution: Early cooling, delayed glacial intensification, and implications for the mid-Pleistocene climate transition. Earth Sci. Rev. 123, 173–193.

Merino, M., 1997. Upwelling on the Yucatan Shelf: hydrographic evidence. J. Mar. Syst. 13, 101–121. http://dx.doi.org/10.1016/S0924-7963(96)00123-6.

Miramontes, E., Jouet, G., Thereau, E., Bruno, M., Penven, P., Guerin, C., Le Roy, P., Droz, 1286 L., Jorry, S.J., Hernández-Molina, F.J., Thiéblemont, A., Silva Jacinto, R., Cattaneo, A. 2020. The impact of internal waves on upper continental slopes: insights from the Mozambican margin (southwest Indian Ocean). Earth Surf. Process. Landforms, 45, 1469–1482.

Molinari, R.L., Johns, E., Festa, J.F., 1990. The annual cycle of meridional heat-flux in the Atlantic Ocean at 26.5-degrees-N. Journal of Physical Oceanography 20, 476–482

Mudelsee, M., Schulz, M., 1997. The mid-Pleistocene climate transition: onset of 100 ka cycle lags ice volume buildup by 280 ka, Earth Planet. Sci. Lett. 151 117-123.

Mullins, H.T., Gardulski, A.F., Wise Jr. S.W. and Applegate, J., 1987. Middle Miocene oceanogrpahic event in the eastern Gulf of Mexico: Implications for seismic stratigraphic succession and Loop Current/Gulf Stream circulation. Geological Society of America Bulletin, 98: 702-713.

Mullins, H.T., Gardulski, A.F., Hine, A.C., Melillo, A.J., Wise, S.W., Applegate, J., 1988. Three-dimensional sedimentary framework of the carbonate ramp slope of central west Florida: A sequential seismic stratigraphic perspective. Geological Society of America Bulletin, v. 100, p. 514-533.

Nürnberg, D., Ziegler, M., Karas, C., Tiedemann, R., Schmidt, M., 2008. Interacting Loop Current variability and Mississippi River discharge over the past 400 kyr. Earth and Planetary Science Letters 272, 278-289

Nürnberg, D., Bahr, A., Mildner, T., Eden, C., 2008. Loop Current Variability—Its Relation to Meridional Overturning Circulation and the Impact of Mississippi Discharge. In: Schulz, M., Paul, A., (eds.). Integrated Analysis of Interglacial Climate Dynamics (INTERDYNAMIC), Springer Briefs in Earth System Sciences, 55-62. DOI 10.1007/978-3-319-00693-2_10

Nürnberg, D., Bahr, A., Mildner, T. C. and Eden, C., 2015. Loop Current variability - its relation to meridional overturning circulation and the impact of Mississippi discharge. In: Integrated Analysis of Interglacial Climate Dynamics (INTERDYNAMIC), ed. by Schulz, M. and Paul, A.. Springer Briefs in Earth System Sciences . Springer, Cham, pp. 55-62. ISBN 978-3-319-00692-5 DOI 10.1007/978-3-319-00693-2_10.

Nürnberg, D., Riff, T., Bahr, A., Karas, C., Meier, K., Lippold, J., 2021. Western Boundary Current in relation to Atlantic Subtropical Gyre dynamics during abrupt glacial climate fluctuations. Global Planetary Change. https://doi.org/10.1016/j.gloplacha.2021.103497.

Nürnberg, Dirk (2022): Benthic and planktonic stable isotopes of sediment core M94-481 PC. PANGAEA, https://doi.org/10.1594/PANGAEA.947792

Nürnberg, Dirk (2022): Sedimentation rate and color data of sediment core M94-481 PC. PANGAEA, https://doi.org/10.1594/PANGAEA.947793

Nürnberg, Dirk (2022): Benthic and planktonic stable isotopes and coarse fraction of sediment core M94-480 PC. PANGAEA, https://doi.org/10.1594/PANGAEA.947790

Nürnberg, Dirk (2022): Sedimentation rate and color data of sediment core M94-480 PC. PANGAEA, https://doi.org/10.1594/PANGAEA.947791

Nürnberg, Dirk (2022): Benthic stable isotopes of sediment core M94-482 PC. PANGAEA,https://doi.org/10.1594/PANGAEA.947795

Nürnberg, Dirk (2022): Sedimentation rate and color data of sediment core M94-482 PC. PANGAEA, https://doi.org/10.1594/PANGAEA.947797

O'Dea, A., Lessios, H. A. , Coates, A. G. , Eytan, R. I., Restrepo-Moreno, S. A. , Cione, A. L., Collins, L. S., de Queiroz, A., Farris, D. W. , Norris, R. D., Stallard, R. F., Woodburne, M. O., Aguilera, O., Aubry, M.-P., Berggren, W. A., Budd, A. F., Cozzuol, M. A., Coppard, S. E., Duque-Caro, H., Finnegan, S., Gasparini, G. M., Grossman, E. L., Johnson, K. G., Keigwin, L. D., Knowlton, N., Leigh, E. G., Leonard-Pingel, J. S., Marko, P. B., Pyenson, N. D., Rachello-Dolmen, P. G., Soibelzon, E., Soibelzon, L., Todd, J. A., Vermeij, G. J., Jackson, J. B. C., 2016. Formation of the Isthmus of Panama. Sci. Adv. 2, e1600883

Oey, L.-Y., Lee, H.C., Schmitz, W.J., 2003. Effects of wind and Caribbean eddies on the frequency of Loop Current eddy shedding: a numerical model study. J Geophys Res 108(C10), 3324

Oey, L.-Y., 2004. Vorticity flux through the Yucatan Channel and Loop Current variability in the Gulf of Mexico. J. Geophys. Res. 109, C10004

Oey, L., Y., 2008. Loop Current and Deep Eddies. Journal of Physical Oceanography, 38, 1426-1447

Paillard, D., Labeyrie, L., Yiou, 1996. AnalySeries 1.0: a Macintosh software for the analysis of geophysical time-series. Eos, Transactions, AGU, 77, 379.

Paull, C.K., Caress, D.W., Gwiazda, R., Urrutia-Fucugauchi, J., Rebolledo-Vieyra, M., Lundsten, E., Anderson, K., Sumner, E.J., 2014a. Cretaceous–Paleogene boundary exposed: Campeche Escarpment, Gulf of Mexico. Marine Geology, 357, 392–400. doi.org/10.1016/j.margeo.2014.10.002.

Pena, L.D., Goldstein, S.L., 2014. Thermohaline circulation crisis and impacts during the mid-Pleistocene transition Science 345 (6194), 318-322. DOI: 10.1126/science.1249770

Pisias, N.G., Moore, T.C., 1981. The evolution of Pleistocene climate: a time series approach, Earth Planet. Sci. Lett. 52 450-458.

Poag, C.W., 2017. Shaken and stirred: Seismic evidence of Chicxulub impact effects on the West Florida carbonate platform, Gulf of Mexico. Geology 45 V.11; 1011–1014 doi:10.1130/G39438.1

Poag, C.W., 2022, Bolide impact effects on the West Florida Platform, Gulf of Mexico: End Cretaceous and late Eocene: Geosphere, v. 18, no. X, 1– 27, https://doi.org/10.1130/GES02472.1.

Prell, W.L., 1982. Oxygen and carbon isotope stratigraphy for the Quaternary of hole 502B: evidence for two modes of isotopic variability, Init. Rep. DSDP 68 (1982) 455-464

Prell, W.L., Imbrie, J., Martinson, D.G., Morley, J.J., Pisias, N.G., Shackleton, N.J., Streeter, H.F., 1986. Graphic correlation of oxygen isotope stratigraphy application to the Late Quaternary. Paleoceanography and Paleoclimatology, 1(2), 137-162.

Quayyum, F., Betzler, C., Cataneanu, O., 2017. The Wheeler diagram, flattening theory, and time. Marine and Petroleum Geology 86, 1417-1430.

QGIS Development Team (2009). QGIS Geographic Information System. Open Source Geospatial Foundation Project. http://qgis.osgeo.org.

Railsback, L.B., Gibbard, P.L., Head, M.J., Voarintsoa, N.R.G., Toucanne, S., 2015. An optimized scheme of lettered marine isotope substages for the last 1.0 million years, and the climatostratigraphic nature of isotope stages and substages. Quaternary Science Reviews 111, 94-106.

Raymo, M.E., Ruddiman, W.F., Shackleton, N.J., Oppo, D.W., 1990. Evolution of Atlantic pacific delta-C-13 gradients over the last 2.5 my. Earth Planet Sci. Lett. 97, 353-368. https://doi.org/10.1016/0012-821X(90)90051-X.

Raymo, M.E. Oppo, D.W., Curry, W., 1997. The mid-Pleistocene climate transition: a deep sea carbon isotopic perspective, Paleoceanography 12, 546-559.

Rebesco, M., 2005. Contourites. In: Selley, R.C., Cocks, L.R.M., Plimer, I.R. (Eds.), Encyclopedia of Geology. Elsevier, Oxford, pp. 513–527.

Rebesco, M., Hernaandez-Molina, F.J., van Rooij, D., Wählin, 2014. Contourites and associated sediments controlled by deep-water circulation processes: state-of the-art and future considerations. Mar. Geol. 352, 111-154.

Reißig, S., Nürnberg, D., Bahr, A., Poggemann, D.-W., Hoffmann, J., 2019. Southward displacement of the North Atlantic subtropical gyre circulation system during North Atlantic cold spells. Paleoceanogr. Paleoclimatol. 34 https://doi.org/10.1029/ 2018PA003376.

Rivas, D., Badan, A., Ochoa,J. , 2005. The ventilation of the deep Gulf of Mexico. Journal of Physical Oceanography 35, 1763-1781

Rubino, A., Falcini, F., Zanchettin, D., Bouche, V., Salusti, E., Bensi, M., Riccobene, G., De Bonis, G., Masullo, R., Simeone, F., Piattelli, P., Sapienza, P., Russo, S., Platania, G., Sedita, M., Reina, P., Avolio, R., Randazzo, N., Hainbucher, D., Capone, A., 2012. Abyssal undular vortices in the Eastern Mediterranean basin. Nat. Commun. 3, 834.

Ruddiman, W.F., Raymo, M.E., Martinson, D.G., Clement, B.M., Backman, J., 1989. Pleistocene evolution: northern hemisphere ice sheets and North Atlantic Ocean, Paleoceanography, 4 353-412.

Sanford, J.C., Snedden, J.W., Gulick, S.P.S., 2016. The Cretaceous-Paleogene boundary deposit in the Gulf of Mexico: large-scale oceanic basin response to the Chicxulub impact. J. Geophys. Res. Solid Earth 121 (3), 1240–1261. https://doi.org/10.1002/2015JB012615.

Schlager, W., Reijmer, J.J.G., Droxler, A., 1994. Highstand shedding of carbonate platforms. Journal of Sedimentary Research 64 (3b), 270–281.

Schmidt, C. , Hensen, C. , Wallmann, K. , Liebetrau, V., Tatzel, M., Schurr, S. L., Kutterolf, S. , Haffert, L., Geilert, S. , Hübscher, C. , Lebas, E. , Heuser, A. , Schmidt, M. , Strauss, H. , Vogl, J. and Hansteen, T. (2019) Origin of high Mg and SO4 fluids in sediments of the Terceira Rift, Azores – indications for caminite dissolution in a waning hydrothermal system. Open Access Geochemistry, Geophysics, Geosystems, 20. DOI 10.1029/2019GC008525.

Schmieder, F., v. Dobeneck, T., Bleil, U. 2000. The Mid-Pleistocene climate transition as documented in the deep South Atlantic Ocean: initiation, interim state and terminal event. Earth and Planetary Science Letters, 179 (3-4), 539-549. doi:10.1016/S0012-821X(00)00143-6

Schmitz, W.J., Richardson, P.L. (1991) On the Sources of the Florida Current. Deep-Sea Research 38,379-409

Schott, F.A., Lee, T.N., Zantopp, R.. 1988. Variability of Structure and Transport of the Florida Current in the Period Range of Days to Seasonal. Journal of Physical Oceanography 18(9), 1209-1230

Serra, N., Ambar, I., Boutov, D., 2010. Surface expression of Mediterranean Water dipoles and their contribution to the shelf/slope-open ocean exchange. Ocean Sci. Discuss. 6, 191–209.

Shackleton, N.J. and Hall, M.A., 1984. Oxygen and carbon isotope stratigraphy of Deep Sea Drilling Project Hole 552A: Plio-Pleistocene glacial history. D~G. Roberts. D. Schnitker et al. Initial Reports of the Deep Sea Drilling Project, 81,599-609. U.S. Govt. Printing Office, Washington.

Sheinbaum, J., Candela, J., Badan, A., Ochoa, J., 2002. Flow structure and transport in the Yucatan Channel. Geophysical Research Letters, 29, NO. 3, 1040, 10.1029/2001GL013990

Slowey, N.C., Curry, W.B., 1995. Glacial/interglacial differences in circulation and carbon cycling within the upper western North Atlantic. Paleoceanography and Paleoclimatology 10(4). doi:10.1029/95PA01166

Sturges, W., Evans, J.C., 1983. On the variability of the Loop Current in the Gulf of Mexico. Journal of Marine Research 41, 639-653

Tachikawa, K., Rapuc, W., Dubois-Dauphin, Q., Guihou, A., Skonieczny, C., 2020. Reconstruction of ocean circulation based on neodymium isotopic composition: potential limitations and application to the Mid-Pleistocene transition. Oceanography. https://doi.org/10.5670/oceanog.2020.205.

Tedesco, K.A. and Thunell, R.C., 2003. Seasonal and interannual variations in planktonic foraminiferal flux and assemblage composition in the Cariaco Basin, Venezuela. J. Foraminiferal Res. 33 (3), 192–210.

Thran, A.C., Dutkiewicz, A., Spence, P., Müller, R.D., 2018. Controls on the global distribution of contourite drifts: Insights from an eddy-resolving ocean model. Earth Planet. Sci. Lett. 489, 228–240.

Tiedemann, R., Sarnthein, M., Shackleton, N.J., 1994. Astronomic timescale for the Pliocene Atlantic δ18O and dust flux records of Ocean Drilling Program Site 659. Paleoceanography and Paleoclimatology, 9(4), 619-638.

Uchupi, E., Emery, K.O.,1968. Structure of continental margin off Gulf Coast of United States. Am Assoc Petroleum Geologists Bull 52, 1162-1193

Wiseman, Jr., W.J., Dinnel, S.P., 1988. Shelf Current Near the Mouth of the Mississippi River. Journal of Physical Oceanography 18(9), 1287-1291

Zavala-Hidalgo, J., Morey. S.L., O'Brian, J.J., Zamudio, L. (2006) On the Loop Current eddy shedding variability. Atmósfera 19, 41-48

Ziegler, M., Nürnberg, D., Karas, C., Tiedemann, R., Lourens, L.J., 2008. Persistent summer expansion of the Atlantic Warm Pool during glacial abrupt cold events. Nature Geoscience 1, 681-685